

UNIVERSITY OF NOVA GORICA

SCHOOL OF APPLIED SCIENCES

**PHOTOEMISSION STUDY OF QUANTUM WELL STATES
OF Co THIN FILM ON Mo(110)**

DIPLOMA THESIS

Luka Novinec

Mentors: doc. Dr. Sandra Gardonio

Dr. Paolo Moras

Nova Gorica, 2013

UNIVERZA V NOVI GORICI
FAKULTETA ZA APLIKATIVNO NARAVOSLOVJE

**PREUČEVANJE KVANTNIH JAM V TANKEM FILMU
Co NA Mo(110)**

DIPLOMSKO DELO

Luka Novinec

Mentorja: doc. Dr. Sandra Gardonio

Dr. Paolo Moras

Nova Gorica, 2013

Acknowledgement

Writing the diploma thesis was my best experience during studying on University of Nova Gorica. Most credits for this goes to my mentor, the person to whom I thank most, doc. Dr. Sandra Gardonio who gave me a lot of support and knowledge needed for finishing diploma thesis and succeed in future. For my experimental part, I'm grateful for help provided by Istituto di Struttura della Materia ISM-CNR group, especially dr. Paolo Moras, Dr. Polina Sheverdyeva and Dr. Alessandro Barla. I very appreciate the opportunity for conducting my experiment at VUV beamline at Elettra Synchrotron Laboratory plus the help and knowledge provided from them during that time. I also thank Dr. Luca Petaccia, for his supervision during my Erasmus Training program at Elettra-Sincrotrone Trieste, and family for patient and support.

Abstract

The growth morphology and the electronic properties of Co thin film on Mo(110) surface has been studied by means of low energy electron diffraction technique and photoelectron spectroscopy using synchrotron light. The growth condition for atomically uniform Co film has been found. Quantum well states of Co film have been observed and characterized by means of angle resolved photoemission. The experimental work has been performed at VUV beamline (ISM-CNR) at Elettra-Sincrotrone Trieste.

Povzetek

Morfologija rasti ter elektronske lastnosti tankega filma Co na površini kristala Mo(110) smo preučevali z uporabo difrakcije elektronov z nizko energijo ter fotoelektronske spektroskopije z sinhrotronsko svetlobo. Vzpostavili smo pogoje za atomsko enakomerno rast tankega filma Co. Z kotno odvisno fotoemisijsko spektroskopijo smo opazovali ter karakterizirali kvantne jame v tankem filmu Co. Celotno eksperimentalno delo je potekalo na VUV žarkovni liniji inštituta ISM-CNR v sinhrotronu Elettra v Trstu.

Contents

Acknowledgement.....	I
Abstract	III
Pozetek	III
Contents.....	V
List of tables	VI
List of figures	VI
1. Introduction	1
1.1 Motivation for studying quantum well states of Co thin film on Mo(110)...	1
1.2 Electron confinement at the nanometre scale	2
1.3 Growth of atomically uniform Co thin film on Mo(110).	7
2. Experimental set up and characterization techniques	11
2.1 The VUV experimental set up.....	12
2.2 Photoelectron spectroscopy.....	19
2.3 XPS analysis.....	21
2.4 Electronic surface structure: Angle Resolved Photoemission Spectroscopy ...	23
2.5 Qualitative analysis surface structure: the low energy electron diffraction technique.	27
3. Preparation and characterization of Mo(110) surface.....	31
4. Growth and characterization of thin Co film on Mo(110).....	39
5. ARPES study of quantum well states of Co thin film on Mo(110)	47
6. Conclusions	52
Bibliographi.....	53

List of tables

Table 1.1 Free energy γ of some materials, in Jm^{-2} [12].....	8
Table 4.1 Calculated values of Co3p and Mo3d areas and from measured core level spectra.....	45

List of figures

Fig. 1.1 Electron confinement in a quantum film (2D). E vs. k_y and k_z is given by parabolic surfaces displaced of $\frac{\hbar^2\pi^2}{2mL^2}$. The density of states curve $D(E)$ is formed of a series of steps, within a parabolic envelop.....	4
Fig. 1.2 Magnified view of the electronic band structure of Ag and Au near the Fermi level along the [111] direction. The dashed line indicates the valence band maximum of Au, which is also the threshold of confinement for the quantum well states in Ag [17].....	5
Fig. 1.3 Photoemission spectra of Ag thin film of different coverages deposited on Au(1 1 1) surface. The dashed curves indicate the evolution of the $n = 1-3$ quantum well peaks [17].....	6
Fig. 1.4 Forms of different film growth: (a) Volmer–Weber; (b) Frank–van der Merwe growth and (c) Stranski–Krastronov.....	7
Fig. 1.5 Rhombic unit cells of a (111)fcc or (0001) hcp monolayer and a (110) bcc substrate, showing Cartesian axes, crystal directions, angles α and β , nearest-neighbour distances a and b , and diagonal lengths a_x , and b_x [19]. For (111) fcc/(110) bcc interfaces with nearest-neighbour distances b and a , respectively, orientations preferred are those in which the most densely packed rows ([110]) in the fcc (111) plane are parallel to one of the densely packed rows in the bcc (110) plane ([111], [1T1],[001]). The first two are called Kurdjumov-Sachs orientations, the last one the Nishiyama-Wassermann (NW) orientation. Co grows epitaxially on Mo(110) in NW orientation.....	10
Fig. 1.6 A schematic phase diagram for the various LEED patterns of Co overlayer on Mo(110) [7].....	11
Fig. 2.1 Schematic view of experimental set-up used at VUV beamline. The set-up is composed by a load-lock system, a preparation chamber and a measurement	

chamber. The three main parts are separated by vacuum valves. The sample can be transfer from the three chambers without breaking the vacuum.....14

Fig. 2.2 Schematic view of heating station used for the preparation of Mo(110) surface.....16

Fig. 2.3 Schematic view of the Co electron beam evaporator.....17

Fig. 2.4 Magnetisation coil used for magnetising the Co film.....18

Fig. 2.5 Schematic view of photoelectric effect.....19

Fig. 2.6 Mean free path λ of different materials as a function of electron kinetic energy [4].....20

Fig. 3.7 Schematic illustration of the photoemission process in a metal [5].....21

Fig. 2.8 The intensity the intensity of the photoemitted of signal in presence of an overlayer is $I = I_0 e^{-\frac{t}{\lambda}}$ where I_0 is the intensity in the absence of the overlayer.....22

Fig. 2.9 Schematic illustration of photoelectric effect with defined angles and wave vectors of the incident photon and emitted electron [8].....23

Fig. 2.10 Conservation of wave vector component parallel ($k_{||}$) to the surface upon transmission of the emitted electron through the surface [8].....24

Fig. 2.11 Schematic view of hemispherical analyser [8].....25

Fig. 2.12 Schematic view of electron energy analyser with 2D detector for acquisition of photoemission intensity maps.....26

Fig. 2.12 Schematic view of electron energy analyser with 2D detector for acquisition of photoemission intensity maps.....28

Fig. 2.14 Examples of real space superlattices on a substrate with a square lattice and corresponding LEED patterns [5].....30

Fig. 2.15 Examples of real space superlattices on a substrate with a hexagonal lattice and corresponding LEED patterns [5].....30

Fig. 3.4 XPS spectra measured on Mo(110) sample after different sample treatments.....33

Fig. 3.5 LEED pattern measured at the centre (a) and at the border (b) of the Mo(110) sample after annealing at $T \approx 1520\text{K}$ in O_2 ($1 \times 10^{-6}\text{mbar}$) for 10 minutes with subsequent flashing (few seconds) at $T \approx 2270\text{K}$	34
Fig. 3.6 XPS spectra of Mo3d core levels after different sample treatments.....	35
Fig. 3.7 XPS wide spectra of clean Mo(110) surface.....	36
Fig. 3.8 LEED pattern of clean Mo(110) surface.....	37
Fig. 3.9 XPS spectra of Mo3d core level of clean Mo(110) surface.....	38
Fig. 3.10 SCLS caused by d-band narrowing and an electrostatic shift for transition metals with less and more than half filling of the d shell.....	38
Fig. 4.1 LEED pattern of Co after short depositions. Measured with electron energy of 149eV. Arrows indicate the [110] and [1-10] direction of Mo.....	40
Fig. 4.2 LEED pattern after 4 min of total Co deposition. Arrows indicate [001] bcc of Mo and [11-20] hcp of Co in one direction and [1-10] bcc of Mo and [1-100] hcp of Co in other direction. $E=143.5\text{eV}$	41
Fig. 4.3 Reference LEED pattern. (a) The LEED pattern observed from 0.5 ML of Co on Mo(110). The full and the hatched lines represent the Mo and the Co lattice, respectively. Two of the integer order spots are indicated. (b) Real space representation of the Co(0001) and Mo(110) unit cells illustrating the NW oriented growth of the Co film. The constants a for Co and Mo are 2.51 and 3.15 Å, yielding a nearest neighbour ratio $r = b/a$ of 0.92, respectively, while $\alpha = 54.736$ and $\beta = 60.0$ [6].....	41
Fig. 4.4 LEED pattern after final deposition and annealing at low temperature. ($T < 500\text{K}$) $E=141.4\text{eV}$	42
Fig. 4.5 Schematic presentation of epitaxial growth.....	43
Fig. 4.6 XPS spectra after 4min of Co deposition on Mo(110).....	44
Fig. 4.7 Red line represent expected values of the ratio between areas of Co3p and Mo3d core levels versus thickness of Co thin film on Mo substrate. Circles represents measured area ratio from core level spectra.....	45
Fig. 4.8 XPS spectra of Co thin film after 10min deposition interval.....	46
Fig. 5.1 (a) Photoemission intensity map of 5 ML of Co on Mo(110) measured with photon energy 56 eV. (b) Sketch of the surface Brillouin zone of the hcp lattice.....	47

Fig. 5.2 Photoemission intensity maps of 8ML of Co on Mo(110) measured after the deposition of the film at RT (a), after 10 minutes of annealing at 400 K (b) and after a second annealing of 10 minutes at 420 K (c).....48

Fig. 5.3 Photoemission intensity map of 5 ML of Co on Mo(110).....49

Fig. 5.4 Photoemission intensity map of 8 ML of Co on Mo(110).....49

Fig. 5.5 Photoemission intensity map of 12 ML of Co on Mo(110).....50

Fig. 5.6 Photoemission intensity map of 8ML of Co on Mo(110) magnetized UP (a) and DOWN (b). In (c) the magnetization directions with respect to the surface Brillouine zone of the hcp lattice.....51

1. Introduction

1.1 Motivation for studying quantum well states of Co thin film on Mo(110).

The band structure of films of nanometre thickness is often characterized by electron confinement in the direction normal to the surface plane, leading to quantization of the electronic levels. Research on this subject was initially focused on the effect of quantum well states on the charge properties of electrons in nanostructure. Later it was recognized that quantum well states also have an important effect on the spin properties of nanostructures. For example, it was shown that the oscillatory magnetic interlayer coupling in a magnetic sandwich can be attributed to the quantum well in the space layer [13]. In the recent years, with the advent of spintronics, the research efforts have been devoted into the integration of both charge and spin degrees of freedom of electrons for engineering new nanostructured devices [14]. At the present, one of the most important objectives of spintronic research is to develop nanostructures that possess spin-split electronic states.

The electronic properties of Co thin film on W(110) have been studied by means of angle resolved photoelectron spectroscopy [15]. It has been observed that the film support quantum well states strongly modified with respect to the free-standing case with dependence also on the magnetization. The behaviour of the Co quantum well states on W(110) is complex and depends on the interplay of three main effects: the breaking of the hexagonal in-plane symmetry due to the coupling of Co 3d states to the 5d W substrate bands, the spin-orbit effects intrinsic to the Co states, and the spin-orbit interaction of Rashba type induced by the symmetry breaking at the film-substrate interface. We plan to grow Co films on a substrate similar to W(110) but with a lower spin-orbit splitting, such as Mo(110), in order to assess the relative weight of the two spin-orbit mechanisms. The crystalline structure and lattice parameter of the hcp Co films are known to be practically identical on the two substrates. The overall electronic hybridization of Co with Mo(110) and W(110) is similar due to the similar atomic and band structures of the two substrates, while the essential difference is the reduction of spin-orbit interaction in Mo.

Within this context, the main objectives of the experimental work presented in this thesis are:

- preparation and characterization of the Mo(110) surface
- preparation and characterization of the Co thin film on Mo(110) surface
- observation the quantum well states of thin film of Co on Mo(110).

The preparation/characterization of the Co thin film on Mo(110) system is done with well known methodologies developed in surface science: *in-situ* growth of metal film, low electron energy diffraction (LEED) and X-ray photoemission spectroscopy (XPS). The quantum well states study is performed with advanced spectroscopy technique based on synchrotron radiation: angle resolved photoelectron spectroscopy (ARPES). ARPES is an extremely powerful technique for measuring the electronic properties of solids yielding direct information about the occupied states.

The experimental data presented here are considered as preliminary work that was required for the full characterization of the electronic and magnetic properties of Co thin film on Mo(110), which is a wider research project ongoing at VUV beamline at ISM-CNR group [15].

1.2 Electron confinement at the nanometre scale

The electron confinement in a solid can be illustrated in the case of a conductive solid, the free electron model, in which the electrons are treated as a non interacting gas (Fermi gas) that is constrained by the infinite potentials of the walls of the container with dimensions L_x, L_y, L_z (i.e. the model of a trapped particle in a box) [8]. In a solid of nanometre dimensions, there will be quantum confinement in any case where one or more dimensions of the volume that contains the electron gas are comparable to the Fermi wavelength $\lambda_F = 2\pi/k_F$ of the electron.

The electronic band structure of a solid depends on its dimensionality. 0-,1-,2-dimensional (D) materials are those in which crystallite size is negligible in 3-,2-,1-,

dimensions but is not restricted in the remaining direction. In the case of a 3-D material, the crystal is macroscopic in all the spatial directions.

Thin films with thicknesses in the range of a few nanometres supported on a crystalline surface are considered 2-D materials. The motion of the electrons perpendicularly to the film can be described with the model of the particle confined in a 1-D box [16]. Although this is a very crude model, it serves to illustrate the basic ideas. If the confinement is limited to the x axis, the electrons are free to move in the direction of the plane (y and z axes), and the allowed values for the energy of the electrons are given by

$$E_{n_x, n} = \frac{\hbar^2 \pi^2}{2m} \left(\frac{n_x^2}{L_x^2} + 2 \frac{n^2}{L^2} \right) \quad (1)$$

for $L_y = L_z = L$ where n_x, n take values 1,2,3 ..., m is the electron mass, \hbar is the Planck constant and are obtained by solving the corresponding Schrödinger equation. Because the dimensions of L are a number typically 10^7 to 10^9 times larger of L_x dimension (thickness of the film) the energies of the levels, labelled by n_x , exhibit a large difference. E vs. k_y and k_z is given by parabolic surfaces displaced of $\frac{\hbar^2 \pi^2}{2mL^2}$. The density of states curve $D(E)$ is formed by a series of steps within a parabolic envelop.

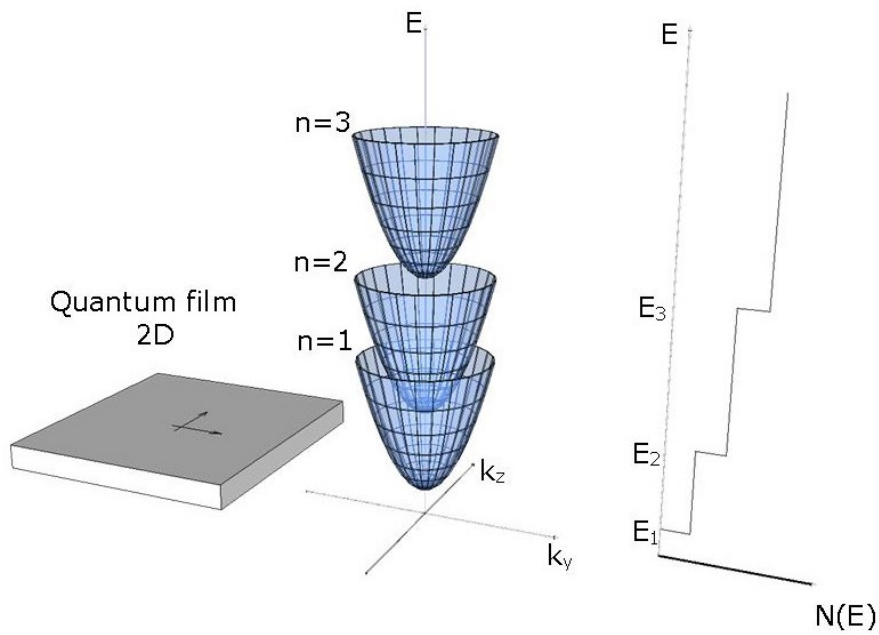


Fig. 11.1 Electron confinement in a quantum film (2D). E vs. k_y and k_z is given by parabolic surfaces displaced by $\frac{\hbar^2 \pi^2}{2mL^2}$. The density of states curve $D(E)$ is formed by a series of steps, within a parabolic envelop.

Note that the quantization condition given in Eq. (1) is valid only for an abrupt infinite barrier. In the case of a thin film supported on a crystalline substrate, the potential barriers that have to be considered are the substrate-film and film-vacuum interfaces. At these two interfaces, the confinement potential is generally finite and rounded and consequently the quantization condition must be modified by considering the correct boundary condition.

A very simple model system that provides a nice illustration of the basic features including the thickness dependence and the effect of the confinement gap in the case of the thin supported film, is represented by the case of epitaxial Ag film on Au(111) [17]. Fig. 1.2 shows a magnified view of the electronic band structure of Ag(111) and Au(111).

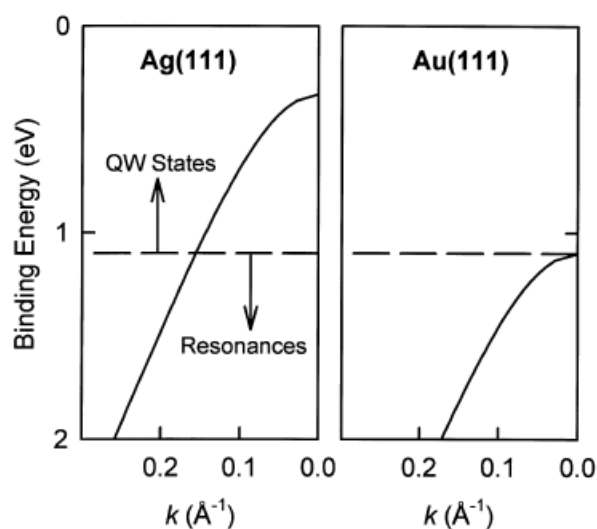


Fig. 1.12 Magnified view of the electronic band structure of Ag and Au near the Fermi level along the [111] direction. The dashed line indicates the valence band maximum of Au, which is also the threshold of confinement for the quantum well states in Ag [17].

The top of the Au *sp* band is of a 1.1 eV binding energy (marked by a horizontal dashed line), compared to 0.3 eV for Ag. Along this particular direction, each crystal looks like a semiconductor with a gap. This relative gap supports an occupied Shockley surface state. Imagine sending an electron with energy within the gap from vacuum towards the crystal surface. The electron cannot propagate inside the crystal and must be rejected backwards. If the energy is also below the vacuum level (work function), the electron cannot escape and is therefore confined. This results in a surface quantum well, which can support a set of quantized states or quantum well states.

A simple test whether the observed states are related to the quantum size effects is to change the film thickness. Eq. (1) shows that as L_x increases, the difference between allowed energy values $E_{n_x, n}$ decrease. In the limit of a very large L_x , the allowed states should form a continuum, and one should recover the band structure of the bulk solid.

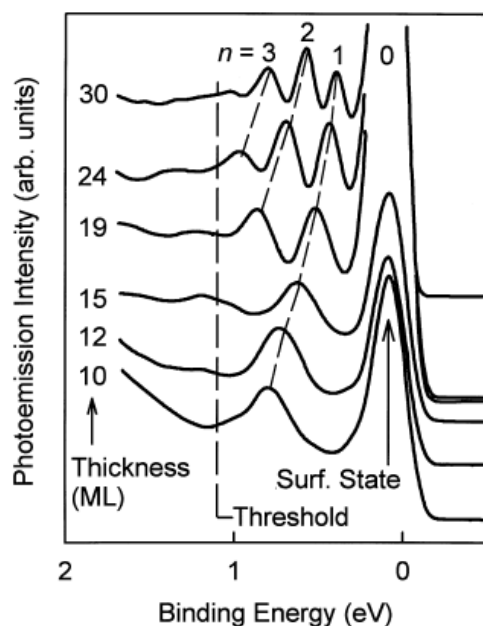


Fig. 1.3 Photoemission spectra of Ag thin film of different coverages deposited on Au(111) surface. The dashed curves indicate the evolution of the $n = 1$ to 3 quantum well peaks [17].

Fig. 1.3 shows a set of normal-emission photoemission spectra for Ag films of various thicknesses. The photoemission spectrum is the fingerprint of the density of occupied states in a sample (see Sec.2.4). Clearly, the peaks become more crowded as the thickness increases, in qualitative agreement with the expectation. As the film thickness increases, the observed quantum well peaks evolve and converge towards the top of the sp valence band. In the limit of an infinitely thick film, one can imagine that the peaks merge to form a continuum. The vertical dashed line in Fig. 1.3 indicates the threshold for confinement. Intense quantum well peaks are observed only to the right of this line. This line, at a binding energy of 1.1 eV, corresponds to the top of the Au sp band (dashed horizontal line in Fig. 1.2). Above this energy, the electrons in the Ag film are located within the relative gap of Au and therefore confined between the Au and surface potentials, forming quantum well states. Below this energy, the electrons can couple to the bulk states in the Au substrate and are therefore unconfined.

1.3 Growth of atomically uniform Co thin film on Mo(110).

An important requirement for the study of quantum well states in thin film is the preparation of atomically uniform film. The elimination of atomic layer fluctuation allows a precise measurement of the quantum confinement effects. In general, it is known that the morphology of the deposit of an atom F on a substrate of element S depends on the surface free energies of F (γ_S) and S (γ_F), as well as on the FS interface energy ($\gamma_{S/F}$) [5]. At thermodynamical equilibrium, the higher the surface energy of the substrate, the stronger the tendency of the element deposited to wet the surface, in other words, to spread or form a homogeneous film.

Forms of film growth for different relative free energies are:

(a) **growth in islands or Volmer–Weber**: 3-D island nucleate and grow directly on the substrate surface

(b) **layer by layer or Frank–van der Merwe** growth: refers to a situation when strictly bi-dimensional layers are grown; the growing layer is fully completed before next one starts to grow

(c) **intermediate or Stranski–Krastonov** growth: after the formation of a complete two-dimensional layer, the growth of three dimensional islands takes place.

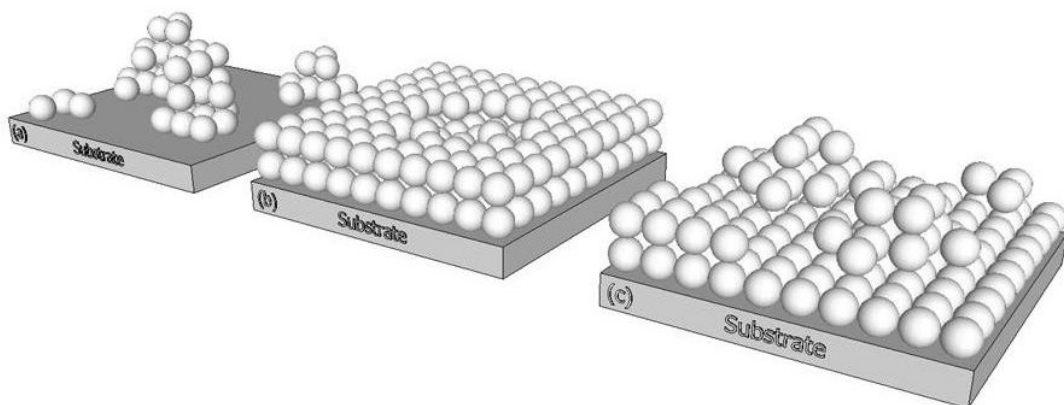


Fig. 1.4 Forms of different film growth: (a) Volmer–Weber; (b) Frank–van der Merwe growth and (c) Stranski–Krastonov.

When the film growth proceeds in layer by layer mode (see Fig. 1.4 (b)) the relation between $\gamma_S, \gamma_{S/F}$, and γ_F is the following

$$\gamma_S \geq \gamma_{S/F} + \gamma_F \quad (2)$$

while in the case of island growth (see Fig. 1.4 (a)) it is the opposite

$$\gamma_S < \gamma_{S/F} + \gamma_F \quad (3)$$

and in the situation when we have layer-plus-island growth, the condition is initially fulfilled for layer-by-layer but when an intermediate layer is formed, the values γ_S and $\gamma_{S/F}$ starts to change, leading to a new condition for which the island growth is favoured. In Table 1.1 we report the surface free energy of some materials [12].

Table 1.2 Free energy γ of some materials, in Jm^{-2} [12].

Magnetic metal	Cr	Mn	Fe	Co	Ni	Gd					
	2.1	1.4	2.9	2.7	2.5	0.9					
Transition metal	Ti	V	Nb	Mo	Ru	Rh	Pd	Ta	W	Pt	
	2.6	2.9	3.0	2.9	3.4	2.8	2.0	3.0	3.5	2.7	
Simple or noble metal	Al		Cu		Ag		Au				
	1.1		1.9		1.3		1.6				
Semiconductor	Diamond		Si		Ge		GaP		GaAs		
	1.7		1.2		1.1		1.9		0.9		
Insulator	LiF		NaCl		CaF ₂		MgO		Al ₂ O ₃		
	0.34		0.3		0.45		1.2		1.4		

In reality the growth of a film does not proceed in thermodynamical equilibrium but is controlled by kinetic parameters. Real surfaces present many defects (steps, adatoms adsorbed from residual UHV gas, vacancies and dislocation, etc.) which provide the additional nucleation centres. Their presence influences the nucleation and diffusion processes. Moreover, the thermal energy of the diffusing atoms depends on the substrate temperature. The supersaturation of the film atoms requires low temperatures or high evaporation rate, on the other hand good crystalline order usually requires high temperatures. Therefore, the film growth is determined by the competition between the influence of defects, substrate temperature and growth rate.

Another important parameter which determines the structure of epitaxially grown film is the lattice misfit $f_{S/F}$ of the film to the substrate defined as the relative difference of lattice parameter of the film (a_F) and the substrate (a_S) respectively:

$$f_{S/F} = \frac{(a_F - a_S)}{a_S} \quad (4)$$

Low misfit (below about 10%) can be accommodated by elastic strain, i.e. deformation of the lattice of the epitaxial film in such a way that the strained film adopts the periodicity of the substrate in the interfacial plane, but can be distorted in the perpendicular direction. This kind of growth is called *pseudomorphic growth*. In addition, the strain energy contributes to the surface energy of the film, and if it becomes larger it could be energetically more favourable to form three dimensional islands on top of the continuous film.

In the equilibrium condition, a Co film is expected to grow on Mo initially in a layer by layer mode. In fact, the Co free energy ($\gamma_{Co} = 2.7 \text{ Jm}^{-2}$, Table 1.1) is lower than the Mo free energy ($\gamma_{Mo} = 2.9 \text{ Jm}^{-2}$, Table 1.1). The growth of Co thin film on Mo(110) surface has been studied in the past with different surface sensitive techniques like LEED, Scanning Tunneling Microscopy and Auger spectroscopy [7, 18, 6, 19], and it is known that Co grows epitaxially on Mo(110) in Nishiyama-Wassermann orientation, i.e. with the hcp Co hexagonal base plane of Co(0001) parallel to Mo(110) (see Fig. 1.5). The Co film has epitaxial strain because of the difference between the Mo lattice parameter ($a_{Mo} = 0.3147\text{nm}$) and that of Co ($a_{Co} = 0.2507\text{nm}$) [18].

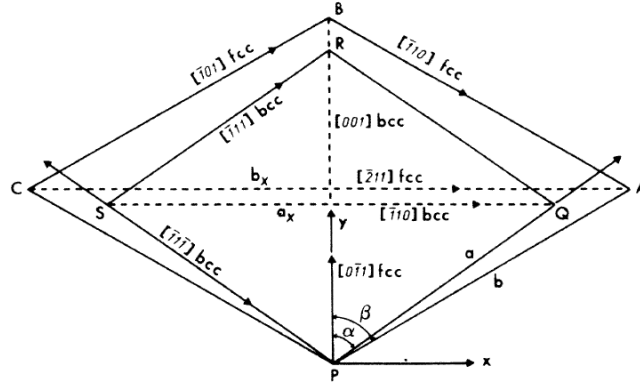


Fig. 1.5 Rhombic unit cells of a (111)fcc or (0001)hcp monolayer and a (110)bcc substrate, showing Cartesian axes, crystal directions, angles α and β , nearest-neighbour distances a and b , and diagonal lengths a_x , and b_x [19]. For (111)fcc/(110)bcc interfaces with nearest-neighbour distances b and a , respectively, orientations preferred are those in which the most densely packed rows ($[110]$) in the fcc (111) plane are parallel to one of the densely packed rows in the bcc (110) plane ($[111]$, $[1\bar{1}1]$, $[001]$). The first two are called Kurdjumov-Sachs orientations, the last one the Nishiyama-Wassermann (NW) orientation. Co grows epitaxially on Mo(110) in NW orientation.

When depositing Co on Mo(110) at room temperature, the Co grows pseudomorphic with the Mo(110) substrate if the Co coverage is below approximately 0.5 monolayer (ML), where 1ML is defined as one pseudomorphic Co layer or, in other words, as the number of atoms in the Mo(110) plane. At Co coverages between 0.5 and 1.2 layers, the Co takes its own close-packed hexagonal lattice instead of that of bcc Mo(110). Any further deposition at room temperature is resulting in forming islands on intermediate layer. With annealing at temperatures above 500K, Co film starts to form in 3D islands [7, 18, 6, 19]. The corresponding LEED patterns of Co overlayers on Mo(110) are complex and depend on Co thickness and annealing temperature of the film (see Fig. 1.6).

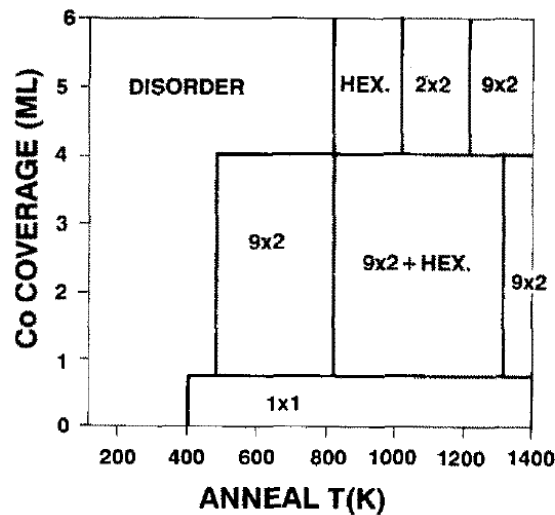


Fig. 1.6 A schematic phase diagram for the various LEED patterns of Co overlayer on Mo(110) [7].

In this thesis, we will focus on the preparation of atomically uniform Co film on Mo(110) for thickness above 4 ML (see Sec. 4.1.2). The reason is that below 4ML the islands formed on the intermediate layer are too small and disconnected, and good quality quantum well states cannot be formed.

2. Experimental set-up and characterization techniques

The main objective of this thesis is the study of the quantum well states of a thin film of Co on Mo(110) surface. The system of the Co film on Mo(110) can be considered as a simple model system, in the sense that it can be characterized by a few definite parameters that are determined from experiments. This is the only way we can hope for some theoretical description which allows us to understand the new properties observed.

For the understanding of the properties of a thin film it is required to know its chemical composition, thickness and crystalline structure. This dictates epitaxial growth of thin film material in a well controlled environment on clean and crystallographically ordered substrate. A fresh, clean surface is usually very reactive with particles, atoms and molecules. Surface gets contaminated by all kind of adsorbed particles which form adlayers on the-top most atomic layer of the solid. Because of disordering and unknown chemical composition of the contamination layer, any further investigation of the sample is prevented.

To ensure good conditions for the experimental study of model systems like thin film on surfaces, first we have to prepare clean, uncontaminated substrate surface. From the characterization point of view it requires surface sensitive spectroscopic and structural techniques like X-ray photoelectron spectroscopy (XPS), angle resolved photoemission spectroscopy (ARPES), and low energy electron diffraction (LEED).

The experimental work presented in this thesis was performed at the VUV Photoemission beamline which is a joint project of Istituto di Struttura della Materia-CNR and Elettra - Sincrotrone Trieste.

The beamline meets all the technical requirements for the study of Co thin film on Mo(110): ultra high vacuum system, high-temperature heating station to prepare the Mo(110) crystal, Omicron evaporation source, magnetizing coil, manipulator operating in the temperature range of 100K to 500K, range of photon energies between 20 and 700 eV in order to study the valence band and core levels. The experimental chamber of VUV beamline is equipped with the Scienta R-4000 WAL analyzer which allows parallel multichannel acquisition over a wide angle range (up to 30°) with variable angular resolution (down to 0.1°), thus providing high quality photoemission maps of the quantum well states of Co thin film.

2.1 The VUV experimental set-up

The characterization of the quantum well states of Co thin film on Mo(110) by means of photoemission spectroscopy relies on the condition that sample surface composition remains essentially unchanged throughout the time required for the measurements. This mostly depends on environment that surrounds the sample. Clean surfaces react with gas species present in the environment, which implies the use of vacuum to reduce the possibility of surface contamination. The concept of vacuum is usually presented in terms of molecular density, mean free path and the time constant to form a monolayer [5]. For calculating the flux I of molecules impinging on the surface, we can use kinetic theory of gases

$$I = \frac{p}{\sqrt{2\pi mk_B T}} \quad (5)$$

Where p is the pressure of gas, m is the mass of molecules, k_B is Boltzmann's constant and T is the temperature. From here, we can easily obtain molecular density n , mean free path λ and time constant to form a monolayer

$$n = \frac{p}{k_B T} \quad (6)$$

$$\lambda = \frac{f}{n\sigma^2} \quad (7)$$

$$\tau = \frac{n_0}{I} = \frac{n_0 \sqrt{2\pi m k_B T}}{p} \quad (8)$$

where σ^2 is molecular cross section and n_0 is number of atoms in a monolayer. At the pressure of high vacuum (HV) which is around 10^{-6} mbar, the mean free path of molecules is ≈ 50 m and contamination layer on fresh, clean surface will form in approximately 2 seconds. For performing photoemission experiments the time required is much higher, so the vacuum has to be higher. We require ultra high vacuum (UHV) ambient at base pressure around 10^{-10} mbar. At this pressure the mean free path of gas molecules is ≈ 50 km and a contamination layer will form in approximately one hour, a time range sufficient to collect a reasonable set of photoemission data on a clean sample.

Another important reason for the necessity of a UHV system is related to the fact that XPS, ARPES and LEED techniques are based on the analysis of low energy electrons ejected or scattered from the sample. The analytical performances are maintained if electrons will reach the corresponding detectors without scattering off of residual gas atoms as well as the formation of a thin "gas (adsorbate) layer" on the surface of the specimen.

To ensure these ambient conditions we performed our experiments in a UHV set-up made of stainless steel continuously pumped by a proper system (see Fig. 2.1).

After mounting the Mo(110) single crystal on a sample holder and placing it inside UHV chamber, we have to air-tight close all openings. This is done by using special copper gaskets between metal flanges to prevent any kind of leaking. After closing the chamber, the pumping process can be initiated.

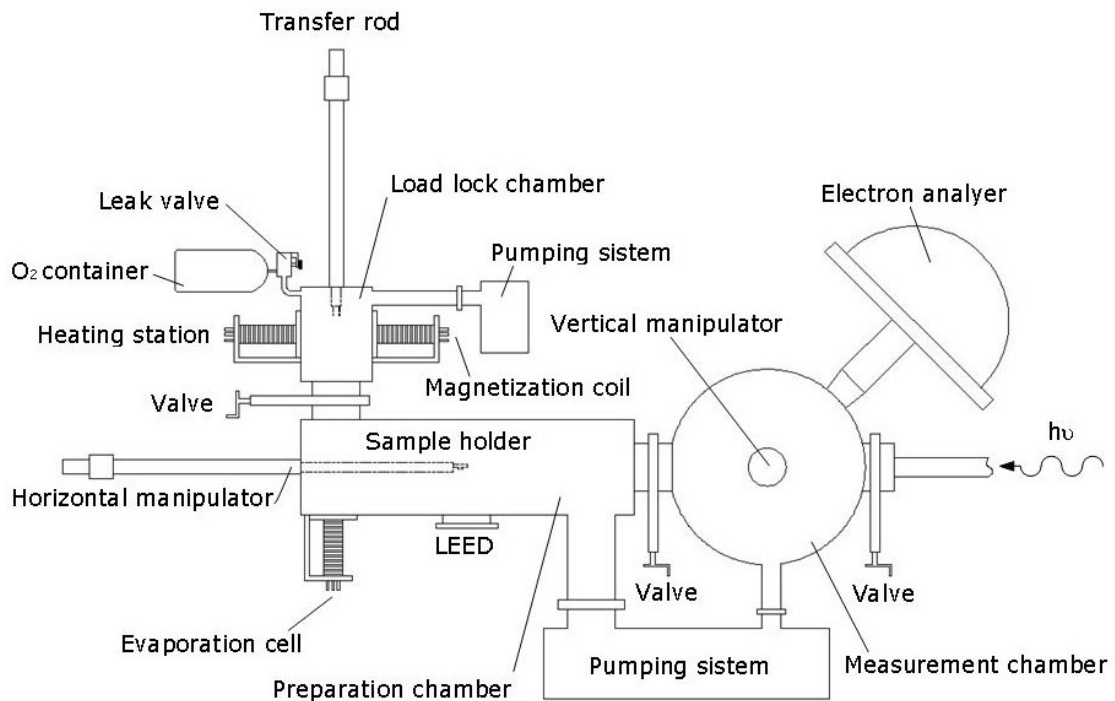


Fig. 2.1 Schematic view of experimental set-up used at VUV beamline. The set-up is composed by a load-lock system, a preparation chamber and a measurement chamber. The three main parts are separated by vacuum valves. The sample can be transferred from the three chambers without breaking the vacuum.

The transition from atmospheric pressure to UHV means changing the pressure value for ≈ 14 orders of magnitude, which is beyond the pumping characteristic of any single pump. So the pumping procedure consists of few different steps involving different pumps and methods to provide UHV conditions. First step is to roughly pump out inside gas to $\approx 10^{-3}$ mbar pressure using rotary pumps. These are simple mechanical pumps which quickly lose their ability because of decreasing density of inside gas. Next step involves so called turbo pumps which helps rotary pumps to reach pressure of high vacuum or $\approx 10^{-6}$ mbar in a relatively short time. Further pumping will provide improving of the vacuum, but reaching the UHV may require long time, since the inside walls get contaminated after being exposed to atmospheric pressure. To remove these contaminants from the inner parts of the chamber, we heat-up the chamber walls above 420K for 1 to 2 days. This results in the evaporation of contaminant species from the surfaces of the inner parts, which are pumped out by turbo and rotary pumps. The procedure is called “bake out” and speeds up a process which otherwise, at room temperature, would last for weeks. The

last step is switching on ion pump which removes any residual molecules of inside gas and maintain UHV at 10^{-10} mbar. Before starting the experiment, the gas composition of the UHV chamber is analyzed using a gas spectrometer.

After good UHV conditions are established we performed the preparation of the sample and we characterized it.

The cleaning of the Mo(110) substrate was performed into the load lock chamber, the small size of which allows us to recover the pressure in a relatively short time. The cleaning procedure (see Sec. 3) requires annealing of the sample up to 2000 K and oxidation at a pressure in the range of 10^{-7} mbar. For this purpose we used the homemade *heating station* (see Fig. 2.2). The heating process is based on electron bombardment. The sample is placed into the sample holder with a tungsten filament positioned centrally behind the sample. By passing current through the filament it glows up and starts emitting electrons. The sample is at a positive high voltage (about 1kV) with respect to the filament and collects a certain emission current from the filament of the order of few tens of mA. With the use of an optical pyrometer we calibrated the temperature of the sample for different values of the electrical power onto the sample. The oxygen gas (99% purity) was let into the chamber through a leak valve.

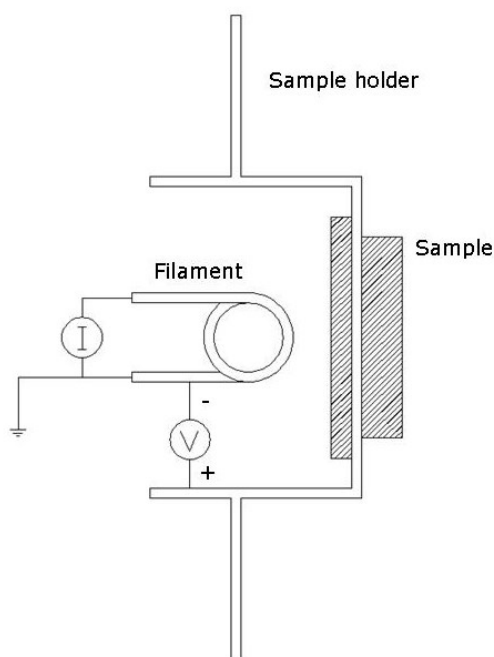


Fig. 2.2 Schematic view of heating station used for the preparation of Mo(110) surface.

To evaluate the cleaning progress on the sample surface, the sample is transferred from the load lock to the preparation chamber using the transfer rod. The horizontal manipulator allows positioning the sample in front of the different instruments present in the preparation chamber (LEED apparatus, evaporator, etc.) and transferring it into the experimental chamber (electron analyzer).

The Co thin film of was evaporated onto clean Mo(110) surface using an *e-beam evaporator* (see Fig. 2.3) maintaining the substrate at room temperature. A high purity (99.99%) Co rod (1 mm diameter) is bombarded with electrons given off by a charged tungsten filament. The electron beam causes atoms from the rod target to transform into the gaseous phase. The rod and the filament are positioned inside of a water cooling shield that reduces degassing effects. By opening the shutter, a flux of Co atoms will reach the surface of the sample that is positioned in front of the evaporator and then Co atoms condense on the surface forming a thin film. Before growing the film, the Co rod must be degassed to get rid of all contaminations that could deposit while it was not used, which involves heating the rod to low temperature.

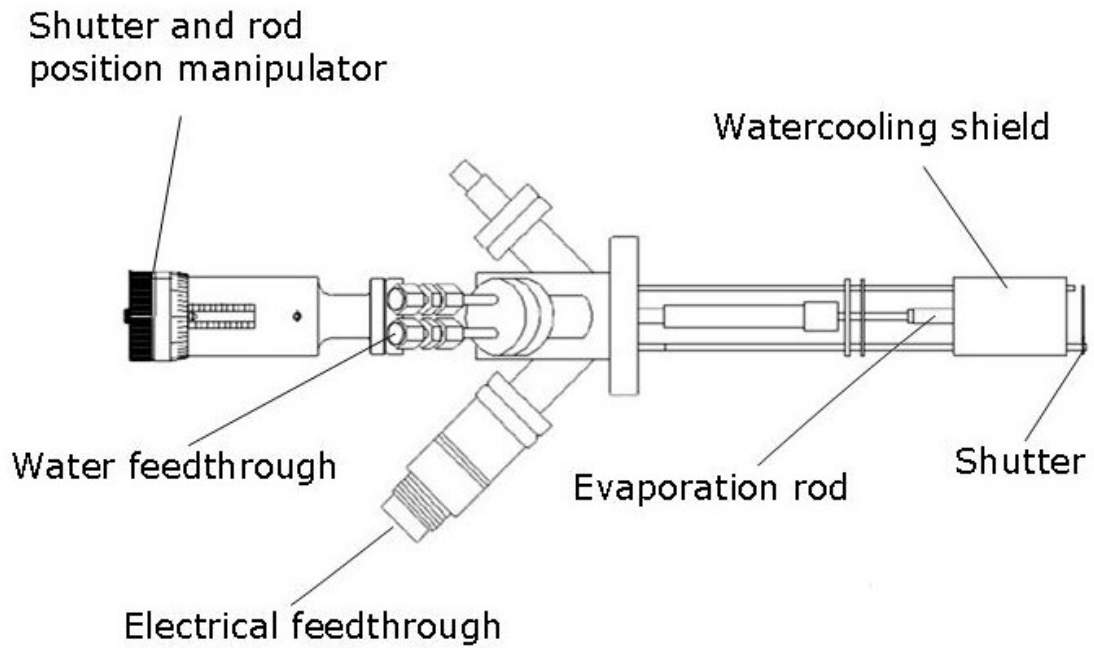


Fig. 2.3 Schematic view of the Co electron beam evaporator.

To obtain good crystalline quality of the Co film, after the deposition we annealed it to about 500 K by passing direct electrical current through the sample holder, kept on the horizontal manipulator.

In our experiment, magnetisation of sample was needed to determine changes of quantum wells versus magnetization orientation. A *magnetisation coil* mounted in load lock chamber was used to magnetise Co film in two opposite directions (M_{up} and M_{down}) depending on the direction of current flowing through coil (see Fig. 2.4).

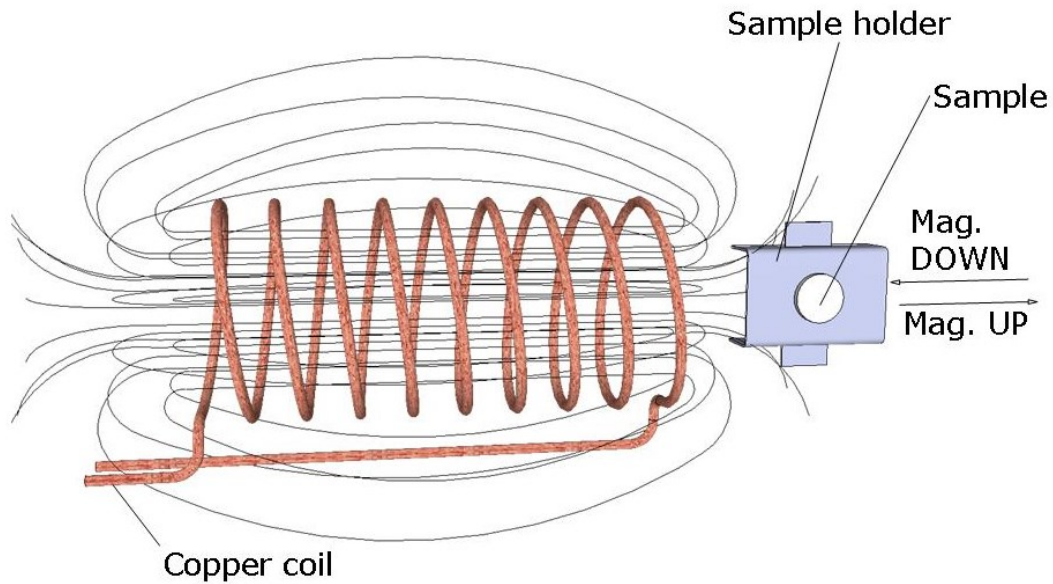


Fig. 2.4 Magnetisation coil used for magnetising the Co film.

The structural characterization was performed by measuring the LEED pattern in the preparation chamber (see Fig. 2.1 and Sec. 2.5). The electronic properties and the chemical composition were measured by means of XPS and ARPES technique (see Sec. 2.3 and Sec. 2.4) using the electron spectrometer Scienta R4000 in the measuring chamber (see Fig. 2.1) and the synchrotron light source of the VUV beamline [20].

The light source of VUV beamline is an undulator with a range of 17 to 900 eV, while the minimum energy at a ring energy of 2.4 GeV is about 25 eV. Between 100 and 900 eV, the measured flux on the sample varies from 1.4×10^{13} to 5×10^{10} photons/sec/0.1%bw/200mA, in a spot of maximum size 0.5 mm. The Kirkpatrick-Baez entrance optics focus the light after which it enters the entrance slit of the monochromator. The monochromator is a Spherical Grating Monochromator with five interchangeable gratings and pre- and post-focusing optics. The set of five gratings provides a resolving power ($R = \lambda/d\lambda$ where $d\lambda$ is the difference in wave length between two spectral lines of equal intensity) of 10,000 over the whole energetic range. The light emerges from the movable exit slit and is then refocused by a post-focusing mirror onto the sample. The beamline is controlled by the Beamline Control System (BCS) except for the monochromator (including the

entrance optics and the exit slit position) which is under the experimental station software control.

2.2 Photoelectron spectroscopy

Photoelectron spectroscopy (PES) is a method used to probe the electronic structure of surfaces and near-surface region. It is a technique based on the *photoelectric effect* (see Fig. 2.5).

This effect occurs, when an electron in a state of binding energy E_i absorbs photon with energy $\hbar\omega$ and escape the solid with kinetic energy E_{kin} .

$$E_{kin} = \hbar\omega - E_i - \Phi \quad (9)$$

where Φ is the work function of the material ($\Phi = E_{vacuum} - E_{Fermi}$).

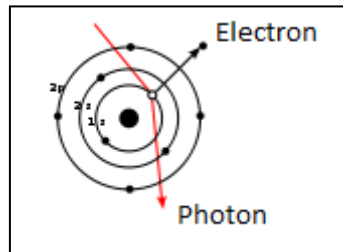


Fig. 2.5 Schematic view of photoelectric effect.

The incoming photons penetrate microns into the surface of the sample. However, the emitted photoelectrons, because of their low kinetic energy (less than 2000 eV), can only travel a short distance without being scattered by colliding or interacting with other atoms and losing energy. This short distance is referred to as the mean free path (λ) of the electron. Mean free path range from 5 to 100Å, depending upon the kinetic energy of the photoelectron (see Fig. 2.6). Photoelectrons that are close enough to the surface to escape without loss of energy will be detected as photoelectron peaks. Those photoelectrons that lose energy before leaving the sample surface will add to the background of the spectrum. This mean free path limitation makes PES a *surface analysis technique* with an average depth of surface analysis of approximately 50Å.

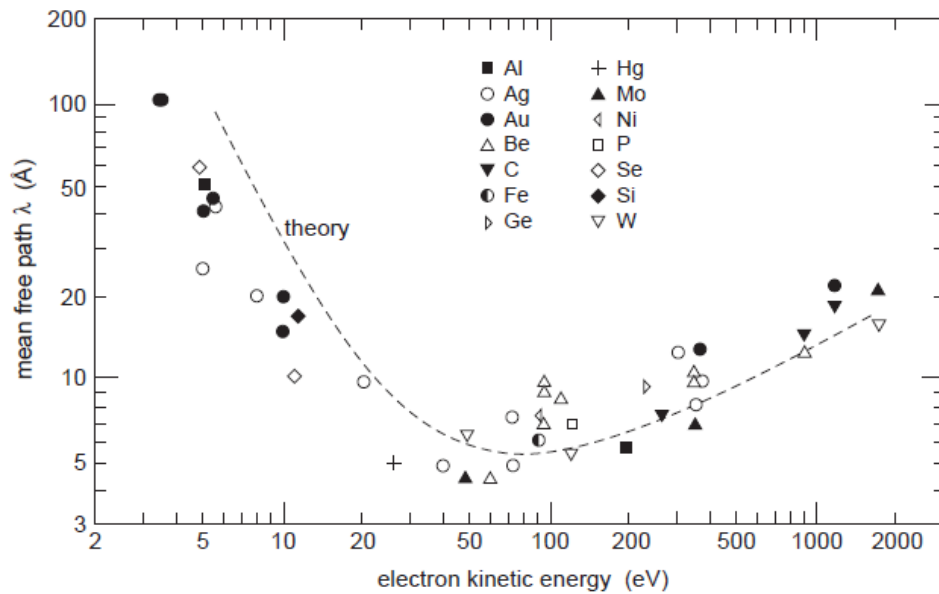


Fig. 2.6 Mean free path λ of different materials as a function of electron kinetic energy [4].

Ejected electrons are collected and analysed by electron-energy analyser and the corresponding angle integrated photoemission spectrum $I(E_K)$ is the fingerprint of the density of occupied states $D(E_i)$ in sample (see Fig. 2.7). In the photoemission spectrum, we clearly distinguish the features due to the electronic excitation from core levels and valence band states and the continuous background of inelastic secondary electrons. In reality the picture is more complex and additional features can be present like for example Auger peaks.

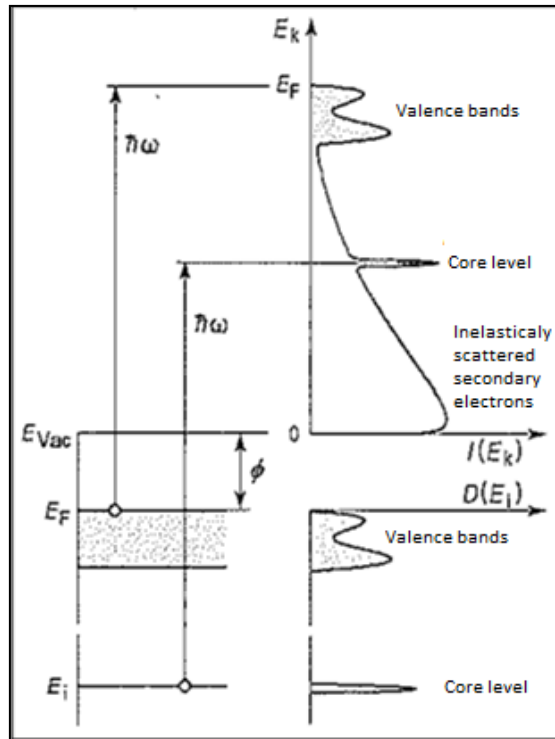


Fig. 13.7 Schematic illustration of the photoemission process in a metal [5].

Depending on the photon energy used for exciting electrons, we can divide photoemission spectroscopy in two groups: X-ray photoemission spectroscopy (XPS) that uses photons in x-ray energy range while ultraviolet photoemission spectroscopy (UPS) uses UV-light.

2.3 XPS analysis

Since binding energies of core electrons are characteristic for elements in a certain chemical environment, XPS allows for a determination of the atomic compositions of a sample or the chemical state of a certain element, as well as electronic structure and band structure. As we will see in the Sec. 3, the chemical shifts can be used to draw direct conclusions on the local coordination in a system and the electronic change upon adsorption. The shape of the spectra and related intensities are determined also by the photoionization cross-section [21] which is different for individual electron level and depends on the photon energy. For example in the case of X-ray, the photoionization cross-section for valence band levels is very low compared to the

one of certain core levels and the result is that the features of valence band in XPS spectra are weaker than this of deep core levels. With use of X-ray photons from synchrotron source, the photon energy can be tuned and there is possibility to select the photon energy for the highest cross-section of a certain electron excitation, maximizing in this way the elemental sensitivity.

XPS can be used for evaluating the thickness of an epitaxial thin film (B) on a substrate (A), by analyzing the core level height. The XPS signal from the underlying substrate will be attenuated (i.e. reduced in intensity) due to inelastic scattering of some of the photoelectrons as they traverse through the layer of material A.

For any single photoelectron, the probability of the electron passing through this overlayer without being subject to a scattering event is given by:

$$P = e^{-\frac{t}{\lambda}} \quad (10)$$

where t is the thickness of the layer of material A and λ is mean free path of the photoemitted electrons.

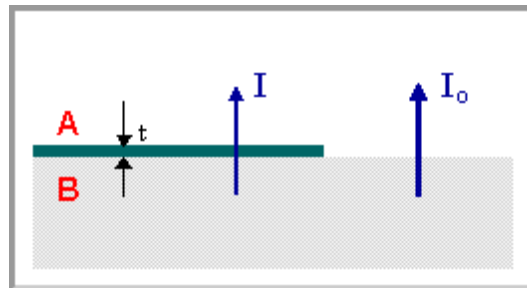


Fig. 2.8 The intensity of the photoemitted signal in presence of an overlayer is $I = I_0 e^{-\frac{t}{\lambda}}$ where I_0 is the intensity in the absence of the overlayer.

It follows that the overall intensity of the XPS signal arising from B is reduced by this same factor, i.e. if the intensity of this signal in the absence of any covering layer is I_0 then the intensity I in the presence of the overlayer is given by:

$$I = I_0 e^{-\frac{t}{\lambda}} \quad (11)$$

These considerations are at the base of the attenuation model that is used in the Sec.4 for the coverage calibration of Co thickness on Mo(110).

2.4 Electronic surface structure: Angle Resolved Photoemission Spectroscopy

By using angle-integrated electron analyzer we get information about the densities of occupied electronic states. In order to investigate the dispersion of electronic bands (E_k) and ($E_{k_{||}}$) for bulk and surface, we have to determine the electron wave vector. Besides the kinetic energy of photoelectrons, we also need to know their emission direction. This method is known as angular resolved photoemission spectroscopy (ARPES).

The kinetic energy of photoemission electron Eq. (1) can be written also as:

$$E_{kin} = \frac{\hbar^2(k_{\perp}^{ex2} + k_{||}^{ex2})}{2m} \quad (12)$$

where k_{\perp}^{ex} and $k_{||}^{ex}$ are the parallel and perpendicular components with respect to surface, of the emitted photoelectron possessing wave vector k^{ex} . In this case wave vector k^{ex} is referred to a free electron in vacuum which is already escaped from solid (see Fig. 2.9).

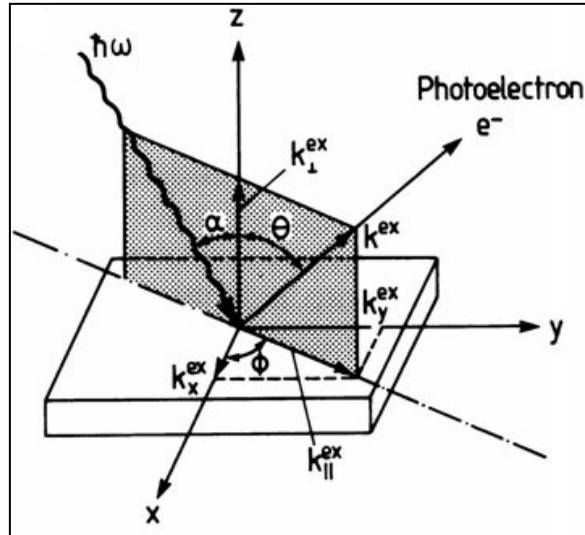


Fig. 2.9 Schematic illustration of photoelectric effect with defined angles and wave vectors of the incident photon and emitted electron [8].

In the case where k^{ex} have the angle of direction θ with respect to the normal of the surface, we can write

$$k_{\parallel}^{ex} = k^{ex} \sin \theta = \sqrt{\frac{2mE_{kin}}{\hbar^2}} \sin \theta \quad (13)$$

We have to consider that when electron is passing through solid-vacuum interface, only the parallel component of the electron momentum is conserved

$$k_{\parallel}^{ex} = k_{\parallel}^{in} + G_{hk} \quad (14)$$

where G_{hk} is a vector in 2D surface reciprocal lattice. In this process, the perpendicular component k_{\perp} is not preserved (see Fig. 2.10).

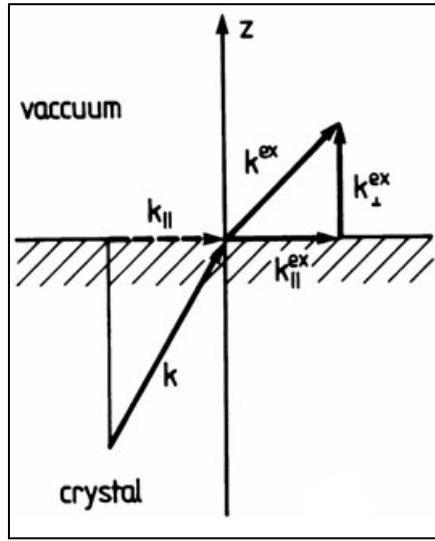


Fig. 2.10 Conservation of wave vector component parallel (k_{\parallel}) to the surface upon transmission of the emitted electron through the surface [8].

The dispersion curve $E_j(k_{\parallel}^{in})$ of a surface state, along a certain surface direction, is experimentally measured recording the photoemission spectra as a function of the polar θ angle while azimuth angle φ being fixed. The information about binding energy E_i and the parallel wave vector component k_{\parallel}^{in} are derived from Eq. (12) and (13) knowing the E_{kin} and θ .

The *experimental set up for photoemission experiments* includes a monochromatic light source, the sample and an electron energy analyzer. In our case the light produced at the undulator is monochromatized in the energy range between 20 and 700 eV while the electron analyzer used is the hemispherical Scienta R-4000 WAL.

In *hemispherical analysers* the electric field formed between two metallic spheres, are balancing the centrifugal force of the electrons on their trajectory (see Fig. 2.11). The hemispherical shape of the electrodes is essential for focusing the beam of electrons. The energy resolution and peak intensity are varying depending on analyser entrance slit size and shape, and the pass energy. The pass energy is basically the kinetic energy of the electrons that are able to pass through the analyser and it's determined by the electrostatic field between metallic hemispheres.

The analyser was operated in so called fixed analyser transmission (FAT) mode where pass energy is held constant. In this way, the spectrum over a broad energy range is obtained by retardation or acceleration of the electrons before they enter the analyser.

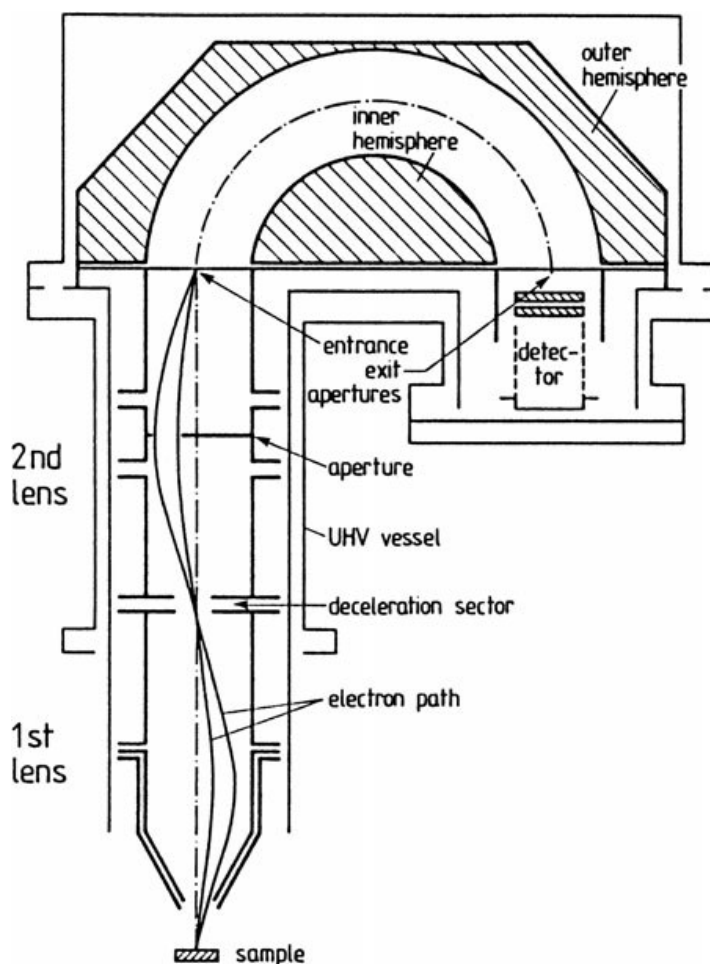


Fig. 2.11 Schematic view of hemispherical analyser [8].

The energy resolution can be calculated as

$$\frac{E_p}{\Delta E} = \frac{2R}{s} \quad (15)$$

where R is the analyser radius, s is the slit width, E_p is pass energy and ΔE is energy resolution of the spectrometer. During our photoemission experiments we used pass energy that corresponds to energy resolution of the analyser of about 5 meV

Electrons passing lenses and electric field of two metallic spheres are detected by 2D detector at the end of the trajectory. The position of each electron on 2D detector is determined by its kinetic energy and emission angle (θ) (see Fig. 2.12). This data is automatically processed by analyser software from where we get photoemission intensity map using the formulas (9) (13) which establish the relation between E_{kin} and E_i , θ and $k_{//}$.

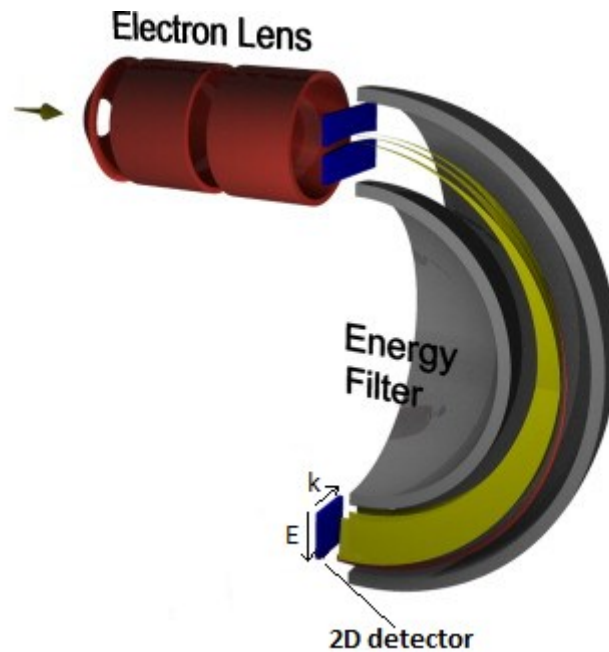


Fig. 2.12 Schematic view of electron energy analyser with 2D detector for acquisition of photoemission intensity maps.

The study of the electronic properties of Co thin film has been done by measuring 2D photoemission intensity maps.

2.5 Qualitative analysis surface structure: the low energy electron diffraction technique.

Low energy electron diffraction (LEED) is well known diffraction technique for the study of surface crystalline structures. The utility of LEED comes mainly from two reasons. First, the de Broglie wavelength of the electron which is given by

$$\lambda = \frac{h}{\sqrt{2mE}} \quad (16)$$

where h is Planck constant and square root of electron mass and energy represents momentum. With typical energy range used in LEED setups, 30 to 200eV, the electrons have a wavelength of $\approx 1-2\text{\AA}$ which fits very well with the typical distances in crystals for satisfying diffraction condition. Second, the mean free path (see Fig. 2.6) of the low energy electrons is very short and consequently most of the elastic collisions take place on the top most atomic layers.

We used a conventional LEED experimental set-up composed by:

- an electron gun which produces collimated beam of low energy electrons
- hemispherical fluorescent screen with a set of four grids to observe the diffraction pattern of elastically scattered electrons
- and sample holder with the sample.

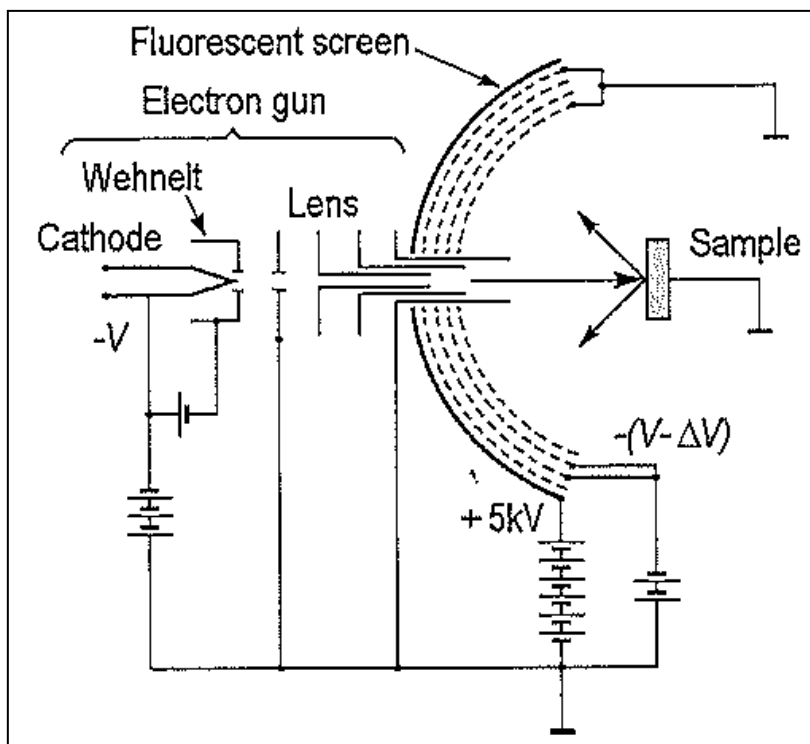


Fig. 2.13 Schematic diagram of the standard four-grid LEED set-up [5].

The cathode filament of the electron gun unit is placed in front of electrostatic lenses (see Fig. 2.13). The cathode is at negative potential while the last aperture, sample and the first grid are grounded. Electrons that are emitted by cathode are accelerated, inside the electron gun. After passing last aperture, electrons are propagating and emitting from sample in the direction of grids in field free space. The potential of the second and third grid is close to that of the cathode filament but lower in magnitude ($-(V-\Delta V)$) and are used to reject inelastically scattered electrons. With changing ΔV , we can adjust brightness of the LEED pattern but also background intensity changes in the same manner. So, the voltage is adjusted to get a LEED pattern with the highest spot-to-background contrast. The fourth grid is used to screen other grids from the field of the fluorescent screen, which is biased to a high voltage of about +5kV, so it must be at ground potential as well. The high voltage of the screen is responsible for reaccelerating the electrons once they pass the second and third grid. Reaccelerated electrons at high energy are causing fluorescence of the screen and the diffraction pattern can be observed.

The discussion of diffraction from a two-dimensional lattice is very similar to that of a three dimensional crystal. In the three dimensions the diffraction pattern is directly related to the crystal reciprocal lattice by the condition [22]

$$k - k_o = G_{hkl} \quad (17)$$

where k is scattered wave vector, k_o is incident wave vector and G_{hkl} is reciprocal lattice vector. In the case of elastic scattering, than

$$|k| = |k_o| \quad (18)$$

The equation (13) and (14) express the laws of conservation of momentum and energy. In the case where we have diffraction from 2D surface, the crystal periodicity in the direction normal to the surface is lacking and (13) transform into:

$$k^{\parallel} - k_o^{\parallel} = G_{hk}. \quad (19)$$

because the wave vector component normal to the surface is not conserved.

Vector of the 2D surface reciprocal lattice G_{hk} must be equal to the scattering vector component parallel to the surface. The LEED pattern gives access to the reciprocal lattice of the surface.

Surfaces are the result of bulk truncation. The crystal surface after truncation is tending to reduce surface free energy. Because of that, the top most layer of atoms rearrange in a way that surface free energy is as low as possible. Rearrangement is possible in two different ways on which mostly effects direction of truncation and temperature of the crystal. In the case that *surface is relaxed* the distance between first and second layer is reduced. But there is no change in parallel periodicity or symmetry of the surface. Unlike relaxation, in the case of *surface reconstruction*, there is a change in the periodicity of the surface structure and a superlattice is formed.

If a surface reconstruction is present we establish qualitative measurement of the surface LEED pattern. The relaxation is possible to be evaluated only by means of quantitative analysis of the intensity of the diffraction spots.

The 1x1 LEED pattern is the simplest case. Such a pattern would exhibit a bulk like terminated surface. With forming of superstructure on the surface, some extra spots are appearing on LEED pattern. This spots are called superspots or extraspots in contrast from those of 1x1 patterns which are integer-order or main spots. (see Fig. 2.14 and 2.15)

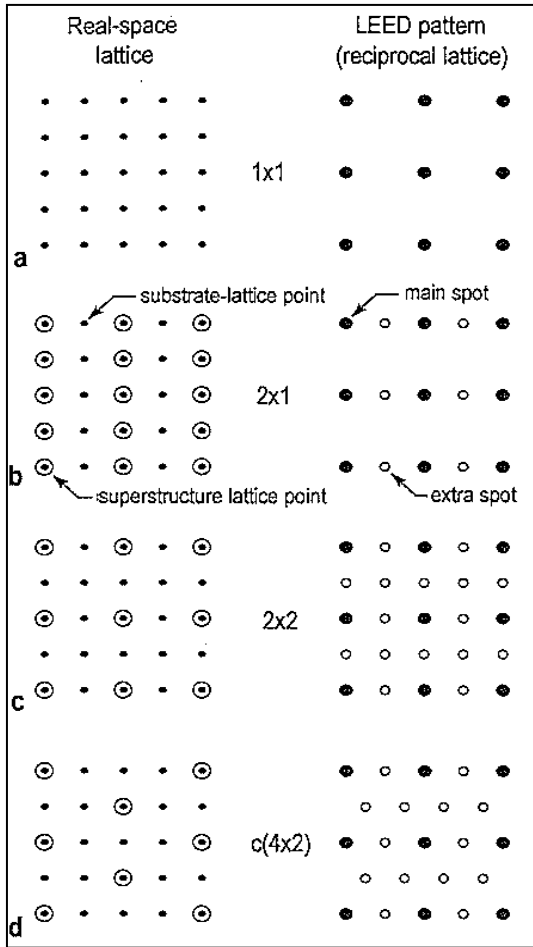


Fig. 2.14 Examples of real space superlattices on a substrate with a square lattice and corresponding LEED patterns [5].

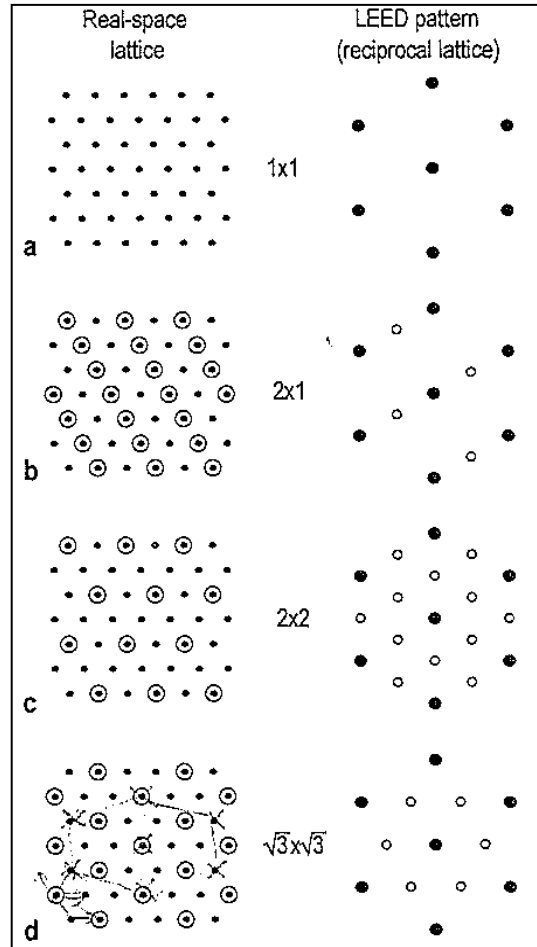


Fig. 2.15 Examples of real space superlattices on a substrate with a hexagonal lattice and corresponding LEED patterns [5].

The crystalline quality of the surface is estimated from sharpness of the spots. Well ordered surface structure with low number of defects results in sharp spots and low background. Any broadening and weakening of the spots plus increasing of the background intensity are consequence of structural defects and crystallographic

imperfections present on crystalline surface. Absence of the LEED pattern is an indication of a disordered, amorphous or finely polycrystalline surface.

In our study we analyzed the LEED pattern qualitatively. We used it for characterizing the preparation of the Mo(110) surface (see Sec. 3). Well prepared Mo(110) surface is not reconstructed (1x1 pattern), but in the presence of O or C contaminants, new superstructures take place (see Sec. 3). Moreover, by evaluating the sharpness of the spots we established the crystalline quality of the Mo(110) after the contamination problems were solved. We used LEED characterization also during the Co film growth on Mo(110) to evaluate the crystalline quality of the surface of the film but also for the determination of the film thickness. As we will describe in the Sec. 4, it is known that the surface of Co thin film grown on Mo(110) possess different surface reconstruction that depends on the Co thickness. We measured the LEED patterns of Co thin film at different thicknesses and we compared them with the phase diagram (see Fig. 1.6) in order to cross check the thickness estimation done with XPS (see Sec. 4).

3. Preparation and characterization of Mo(110) surface

A necessary condition for the observation of quantum well states on a metallic thin film by means of photoemission spectroscopy is that the film grows almost perfectly layer by layer. The body centred cubic (bcc)(110) surface of Mo and W are very suitable substrates for growing magnetic thin films (Fe, Co and Ni), as their free surface energy is high and interdiffusion or surface alloying generally do not occur.

In this chapter we will present the characterization of the Mo(110) clean surface and the growth of Co thin film on Mo(110). The surface and thin film crystalline structure and chemical composition have been analyzed by measuring the LEED patterns and XPS core levels (see Sec. 3) at different stages of their preparation.

Mo(110) crystal surface was prepared following the standard procedure [1]. The procedure consists of annealing the sample in O₂ pressure (1×10^{-7} mbar) at approximately 1500 K and flashing the sample to higher temperature ($T \approx 2000$ K).

This procedure is usually repeated several times until good surface crystalline structure and chemical composition is obtained.

The XPS spectra after the first cycle of treatment (see Fig. 3.1 (a)) presented Oxygen, Carbon and Sulphur contaminants (O 1s core level, C 1s core level and S ($L_{23}M_{23}M_{23}$ Auger line)) together with the Mo core levels ($3p_{1/2}$, $3p_{3/2}$, $3d_{3/2}$, 4s, $4p_{1/2}$, $4p_{3/2}$). The LEED pattern of the sample was not homogeneous over the sample surface. A $p(4 \times 4)$ pattern was present at the centred of the sample (see Fig. 3.2(a)), while at the border it show up a two rows of satellite spots that form and X shape cantered about the molybdenum $p(1 \times 1)$ spots (see Fig. 3.2(b)). The observed reconstruction of Mo corresponds respectively to the molybdenum carbonization [3] ($p(4 \times 4)$) and oxidation ($p(1 \times 1)$) [2].

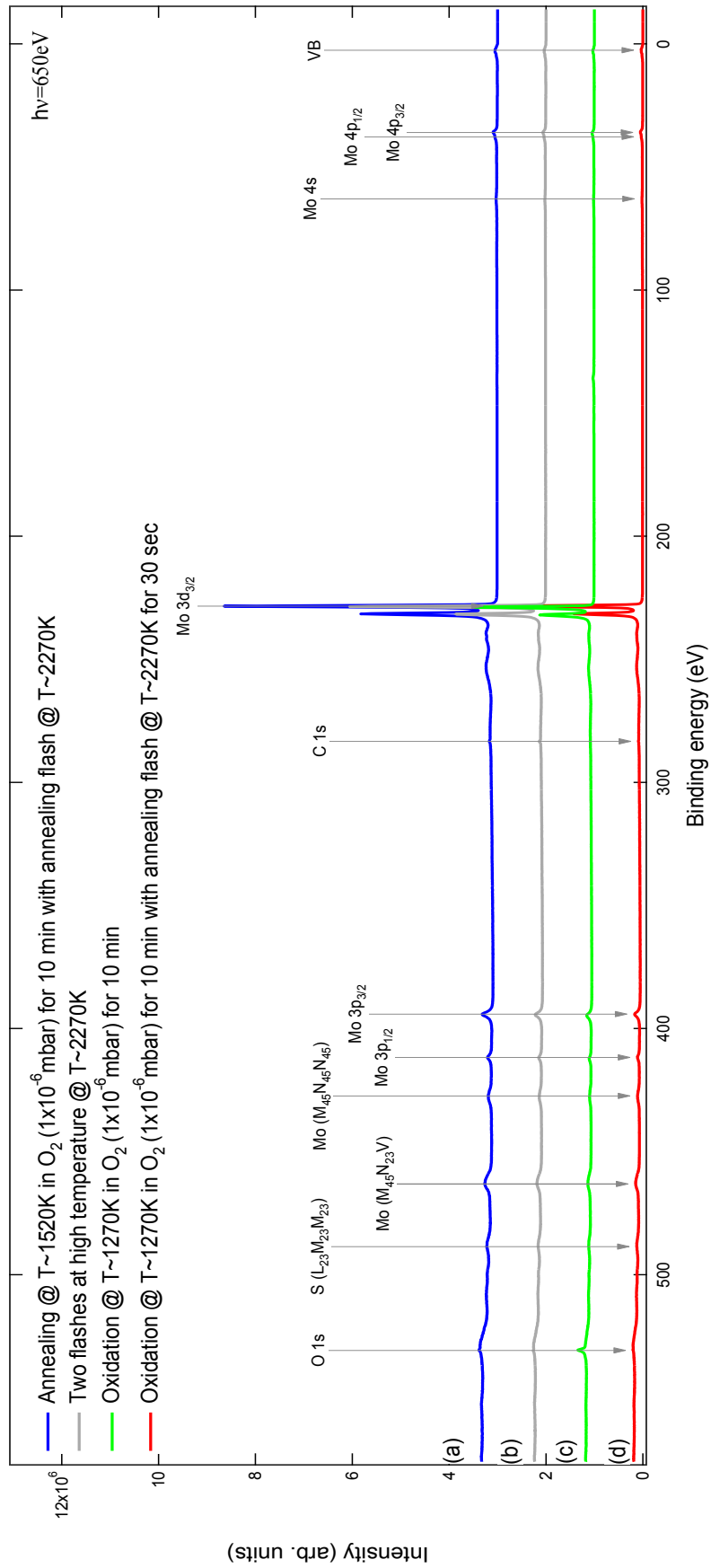


Fig. 3.14 XPS spectra measured on Mo(110) sample after different sample

The non-homogeneous crystalline structure of the surface along the sample surface is a result of non homogeneous annealing of the sample during the final flashing. The sample is heated up by electron bombardment (see Fig. 2.2) and because of the sample dimensions and the heating stage set-up (basically the dimension of the filament behind the sample) the time required for the sample to reach the thermal equilibrium is longer than the flashing time here used. The hottest part corresponds to the position of the filament (centre of the sample) while the coldest is at the border of the sample.

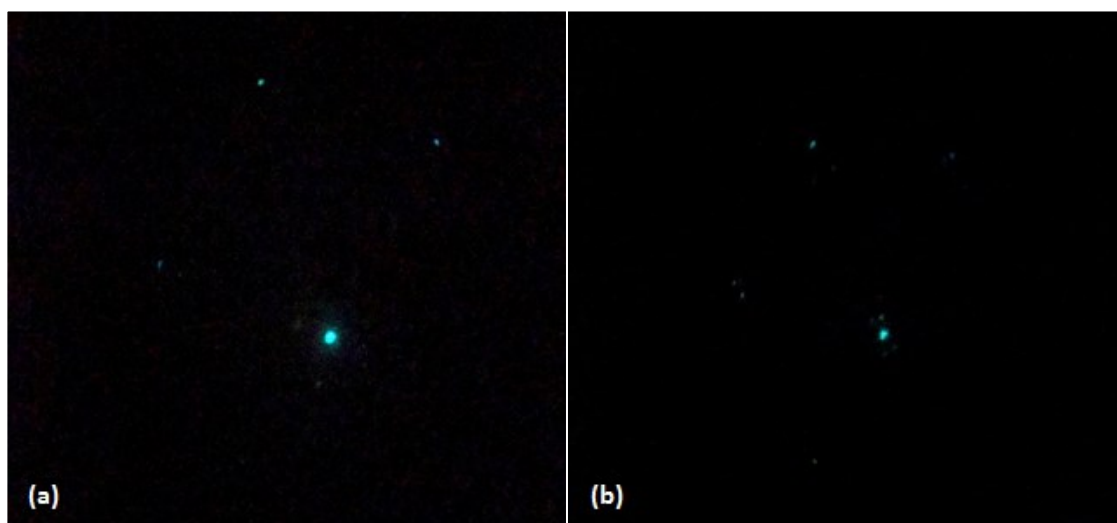


Fig. 3.15 LEED pattern measured at the centre (a) and at the border (b) of the Mo(110) sample after annealing at $T \approx 1520\text{K}$ in O_2 ($1 \times 10^{-6}\text{mbar}$) for 10 minutes with subsequent flashing (few seconds) at $T \approx 2270\text{K}$.

Oxygen contamination is a result of the non complete removal of it after the final flashing (too low temperature at the border of the sample) while C and S, which are known as bulk contaminants of Mo, can diffuse during the final flashing at too high temperature. We confirm these hypotheses by measuring the XPS spectra after two flashes at high temperature ($T \approx 2270\text{K}$) (see Fig. 3.1(b)) and after an oxidation at $T \approx 1270\text{K}$, with oxygen pressure of $1 \times 10^{-6}\text{mbar}$ for 10 minutes (see Fig. 3.1(c)).

After the flashing at high temperature the C contamination increases with respect to the one after the complete preparation cycle (compare spectra in Fig. 3.1(c) and Fig. 3.1(a)). For better understanding we also measured the Mo 3d core level spectra, with 300 eV photo energy, and compare it with the one measured after the first cycle

of Mo(110) preparation (Fig. 3.3(a)). We observed that the two flashes at high temperature do not change the line shape of the Mo 3d core level (Fig. 3.3(b)).

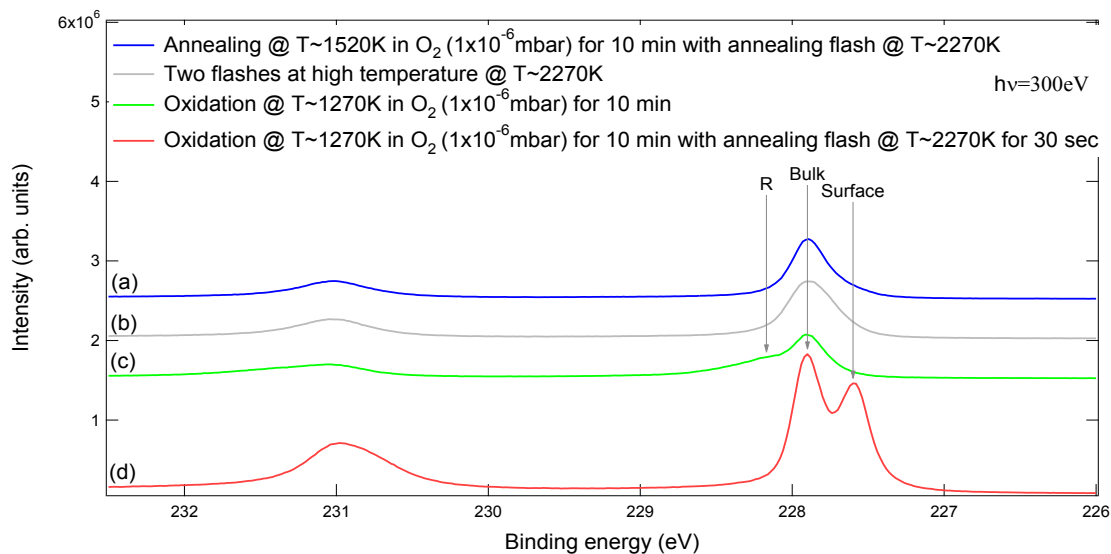


Fig. 3.16 XPS spectra of Mo3d core levels after different sample treatments.

The subsequent oxidation provokes the strong reduction of C contribution in the XPS spectra (see Fig. 3.4(c)) and a variation of the core level line shape of the Mo 3d (see Fig. 3.3(c)). In Mo 3d core level spectra, we observe the appearance of a structure (R) at about 480meV higher binding energy with respect to the peak observed after previous treatments (Bulk). The new structure is a finger print of Mo oxidation.

Based on these observations, we concluded that in order to eliminate efficiently C contamination we needed to perform the oxidation and the final flash annealing at lower temperature with respect to the first treatment. More efficient oxidation of C on the surface and less amount of C diffusion from the bulk is obtained by lowering the temperature during the oxygen treatment, and final flashing.

Finally, a good surface preparation was obtained by O₂ treatment (1270K, 10min, 1x10⁻⁶mbar) and final flashing (1470K, 30sec) (see Fig. 3.1(d)) No C and S contamination is present and also the residual oxygen contribution is very low. The strong reduction of S contamination most probably is due to the fact that like in the case of C, we reduce its diffusion from the bulk by lowering the temperature of the flash annealing.

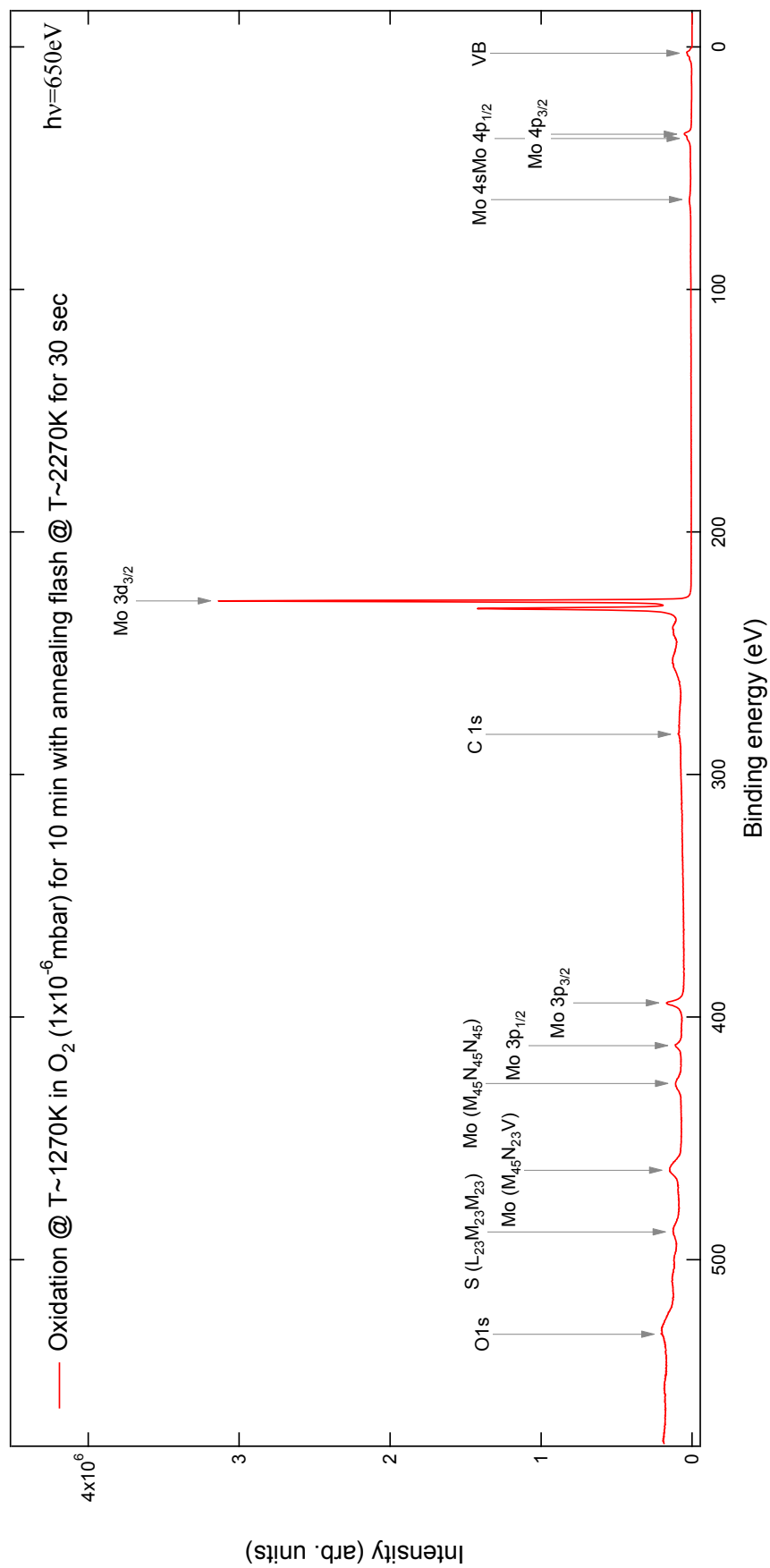


Fig. 3.17 XPS wide spectra of clean Mo(110) surface.

We repeated about five cycle of preparation of Mo(110) using the optimized temperatures of annealing and we observed sharp 1x1 LEED pattern (Fig. 3.5). We measure the XPS spectra (see Fig. 3.4 and 3.6) and we do not detect surface contaminants. The Mo 3d core level spectrum present well resolved structures (labelled as Bulk and Surface) energy shifted by 0.33 eV (see Fig. 3.6).



Fig. 3.18 LEED pattern of clean Mo(110) surface.

The presence of these two components is a finger print of the good quality of the prepared surface of Mo(110). In fact, it is very well known in literature that the high quality Mo(110) surface is characterized by 3d core level spectra composed by two component: bulk and surface [1].

The presence of the two core level component, in the case of transition metal crystals, is ascribed to the fact that when crystal is truncated, the surface atoms have lower coordination number than the bulk due to the smaller number of nearest neighbours. The reduction of the atomic coordination number causes the narrowing of the d-band of the top most layer of the crystal and its energy shifts upwards or downwards with respect to the Fermi level depending if the transition metal have less or more than half filled *d* shell.

Between bulk and surface appears a chemical potential difference or we can say that surface gets positive (more than half filled) or negative (less than half filled) charged.

The related electrostatic potential than shifts core level towards lower or higher binding energies (see Fig. 3.7) [4].

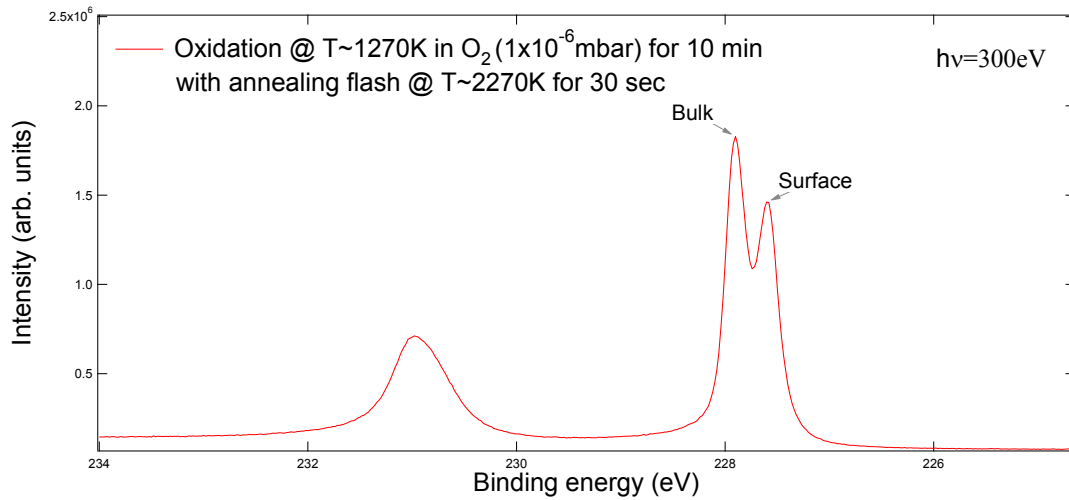


Fig. 3.19 XPS spectra of Mo3d core level of clean Mo(110) surface.

The energy difference between the corresponding surface and bulk is known in literature with the acronym of SCLS (Surface Core Level Shift).

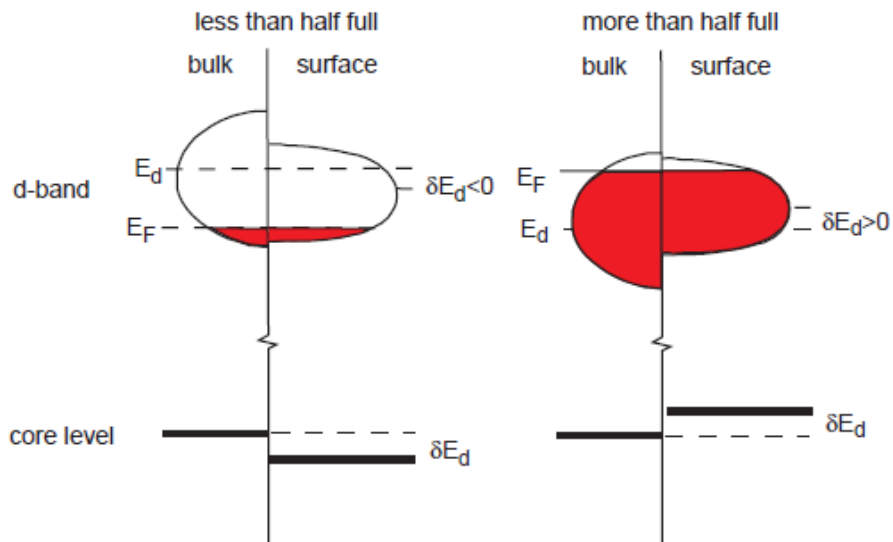


Fig. 3.20 SCLS caused by d -band narrowing and an electrostatic shift for transition metals with less and more than half filling of the d shell.

In Fig. 3.7 we can see shifting of the energy of d -band (E_d) in respect to chemical potential difference between surface and bulk component. Also core levels are shifted for the same δE_d as d -band. Fermi energy (E_F) remains the same regardless of d -band energy transition.

4. Growth and characterization of thin Co film on Mo(110)

One of the objective of this thesis is the growth of an epitaxial film of Co on Mo(110) (see Sec. 1.3).

For that purpose Co was evaporated using the electron bombardment evaporator (see Fig. 2.3) on clean Mo(110). The calibration of the coverage was performed by measuring XPS core level spectra and comparing measured LEED patterns with the previous studies [6, 7].

To ensure the cleanness of the evaporating material the evaporator was out-gassed, prior to the deposition. We deposit Co several times in small intervals keeping constant the Co evaporator parameters. At the beginning the interval was 30 seconds long. Every next interval was two times longer than previous one up to interval duration of 16 minutes.

After one minute of Co deposition, the LEED pattern shows blurred dots ordered in strained hexagonal shape (see Fig. 4.1). The 1×1 LEED pattern here obtained corresponds to the pseudomorphic growth of Co atoms in the coverage regime below 0.5ML [6, 7] (see Sec. 1.3). After a total deposition time of about 4 minutes and subsequent annealing at about 500 K, we observed a LEED pattern with satellites spots along the $[001]$ direction (see Fig. 4.2). The pattern corresponds to a Co coverage in the range of 0.5ML - 4ML observed in previous studies [6, 7]. The structure is designed as 9×2 -like structure that we depict in Fig. 4.3. The 9×2 structure is interpreted to correspond to multiple scattering by the Mo(110) substrate and the Co overlayer. The assignment of the unit cell of Co in reciprocal space (see Fig. 4.3(a)) and real space is shown in Fig. 4.3(b).

The last Co deposition had a total duration of 16 minutes with subsequent annealing at temperature of about 500 K. The corresponding LEED pattern is shown in Fig. 4.4 and the structure is clearly hexagonal with sharp spots. The hexagonal structure here observed differs from the one obtained after short Co deposition (see Fig. 4.1) which correspond to the clean Mo(110) surface. As previously observed [7] the six-fold symmetry indicates that the new hexagonal pattern corresponds to Co clusters with their (0001)-hcp planes parallel to Mo(110). By comparing the LEED pattern in Fig.

4.1 and Fig. 4.4 we observe a difference in the spot distances b_1 , b_2 and b_3 , b_4 . The two patterns are acquired with two different electron energies and we cannot directly compare b_1 and b_2 with b_3 and b_4 , but the fact that the ratio b_1/b_2 is different from b_3/b_4 we conclude that Co film grow strained, as expected [18], with different strain along $[11-20]$ and $[1-100]$ of hcp Co.

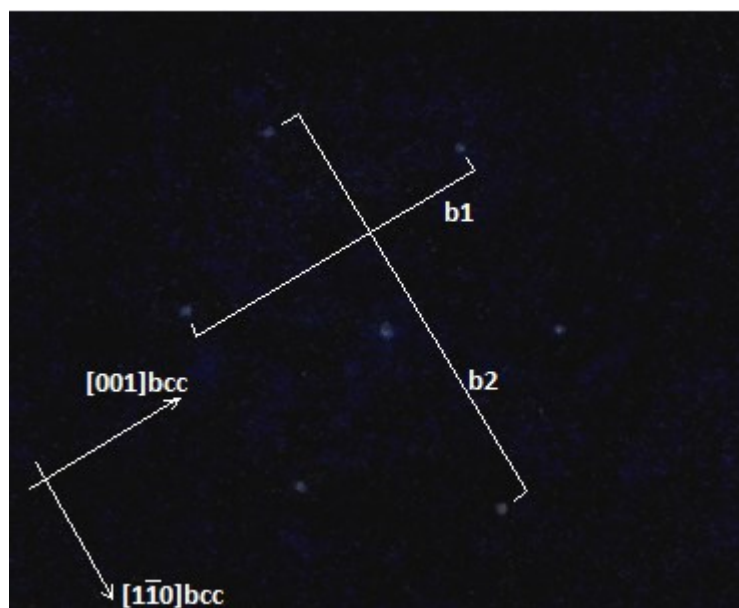


Fig. 4.1 LEED pattern of Co after short depositions. Measured with electron energy of 149eV. Arrows indicate the $[110]$ and $[1-10]$ direction of Mo.



Fig. 4.2 LEED pattern after 4 min of total Co deposition. Arrows indicate $[001]_{\text{bcc}}$ of Mo and $[11-20]_{\text{hcp}}$ of Co in one direction and $[1-10]_{\text{bcc}}$ of Mo and $[1-100]_{\text{hcp}}$ of Co in other direction. $E=143.5\text{eV}$

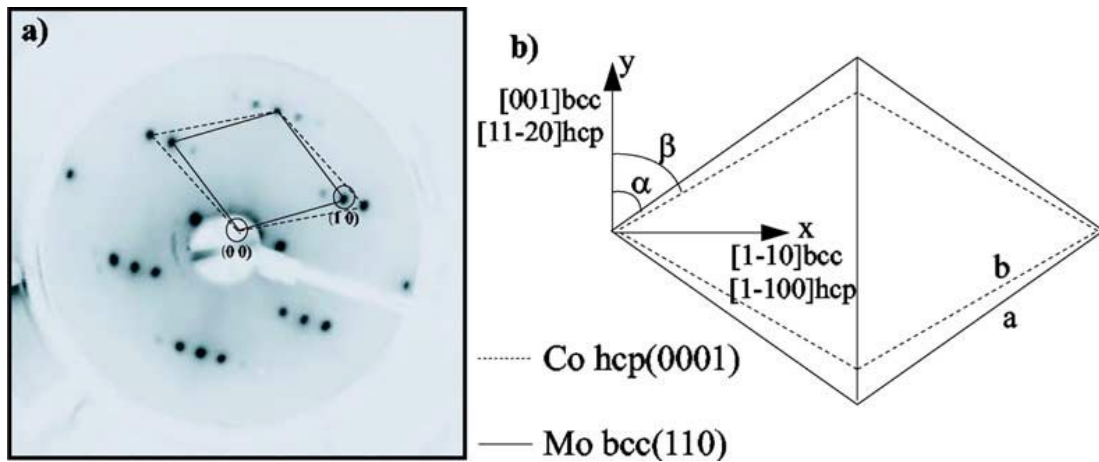


Fig. 4.3 Reference LEED pattern [6]. (a) The LEED pattern observed from 0.5 ML of Co on Mo(110). The full and the hatched lines represent the Mo and the Co lattice, respectively. Two of the integer order spots are indicated. (b) Real space representation of the Co(0001) and Mo(110) unit cells illustrating the NW oriented growth of the Co film. The constants a for Co and Mo are 2.51 and 3.15 \AA , yielding a nearest neighbour ratio $r = b/a$ of 0.92 , respectively, while $\alpha = 54.736$ and $\beta = 60.0$.

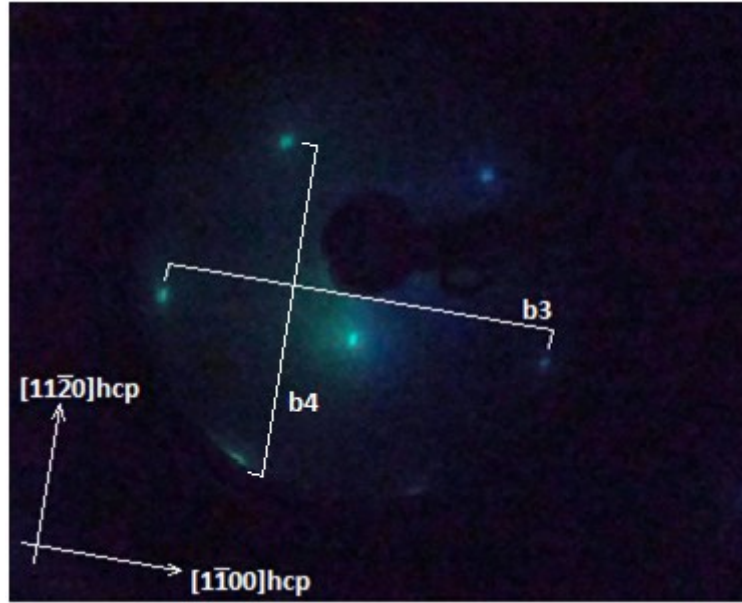


Fig. 4.4 LEED pattern after final deposition and annealing at low temperature. ($T < 500\text{K}$) $E = 141.4\text{eV}$

At the two different coverage regimes we also measured the XPS spectra before and after Co deposition. In Fig. 4.6 are reported the Mo $3d$ and Co $4p$ core spectra after 4 minutes (low coverage regime), while in Fig. 4.8 after 10 minutes (high coverage regime) of Co deposition.

We can estimate the thickness of the deposited Co film on Mo(110) by calculating the intensity ratio of Co $3p$ core level and Mo $3d$ core level and compare with the expected values in the case of a simple attenuation model (see Sec. 2.3). By the following formula is given expected ratio between area of $3p$ core level peak of Co (A_{Co}) and area of $3d$ core level of Mo (A_{Mo}):

$$\frac{A_{Co}}{A_{Mo}} = \frac{\sigma_{Co}}{\sigma_{Mo}} \frac{\sum_{i=0}^n e^{-i \frac{d_{Co}}{\lambda_{Co}}}}{\sum_{i=0}^{\infty} e^{-(i+n) \frac{d_{Mo}}{\lambda_{Mo}}}} \quad (20)$$

which depends on photoelectron escape depth of Co (λ_{Co}) and of Mo (λ_{Mo}), spacing between Co layers (d_{Co}) and Mo layers (d_{Mo}), photoelectron cross section at given energy of Co (σ_{Co}) and Mo (σ_{Mo}) and amount of deposited material (n). We can see that if the coverage of deposited material is increasing, the contribution from substrate is decreasing. As soon as the dimension of deposited material exceeds escape depth of the electron from substrate, we lose contribution from it.

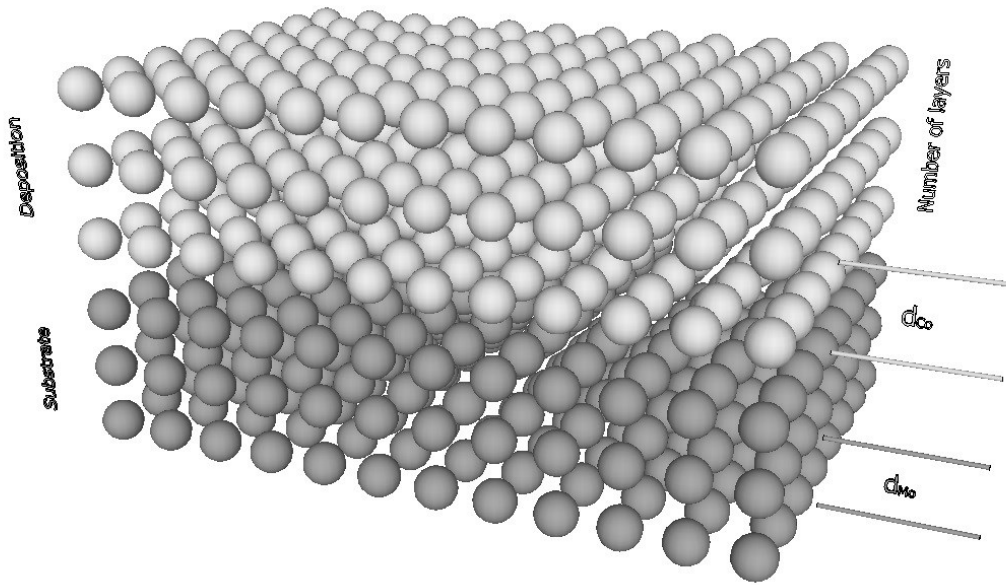


Fig. 4.5 Schematic presentation of epitaxial growth.

In Fig. 4.7 we report the expected values of A_{Co}/A_{Mo} using (20). The coverage of deposited Co on Mo is represented as n as number of deposited monolayers. In Table 4.1 we report the calculated values of the area of the Co $3p$ core level (A_{Co}), Mo $3d$ core level (A_{Mo}) and their ratio (A_{Co}/A_{Mo}) for the two different coverages. By comparing the experimental ratio of A_{Co}/A_{Mo} (see Fig. 4.6 and Fig. 4.8) with the one expected by the model (Fig. 4.7), at the low coverage regime corresponds to about $1.5ML \pm 1ML$ while the high coverage regime corresponds to about $5ML \pm 1ML$. The rough estimation of the coverage of Co in the two regimes by using this simple model is in line with the observation of the LEED pattern. From literature (see Fig. 4.3) is in fact known that the LEED pattern observed in Fig. 4.2 is observable for coverages of ABOVE about $0.5ML$ [7], while the purely hexagonal pattern can be observed only above $4ML$.

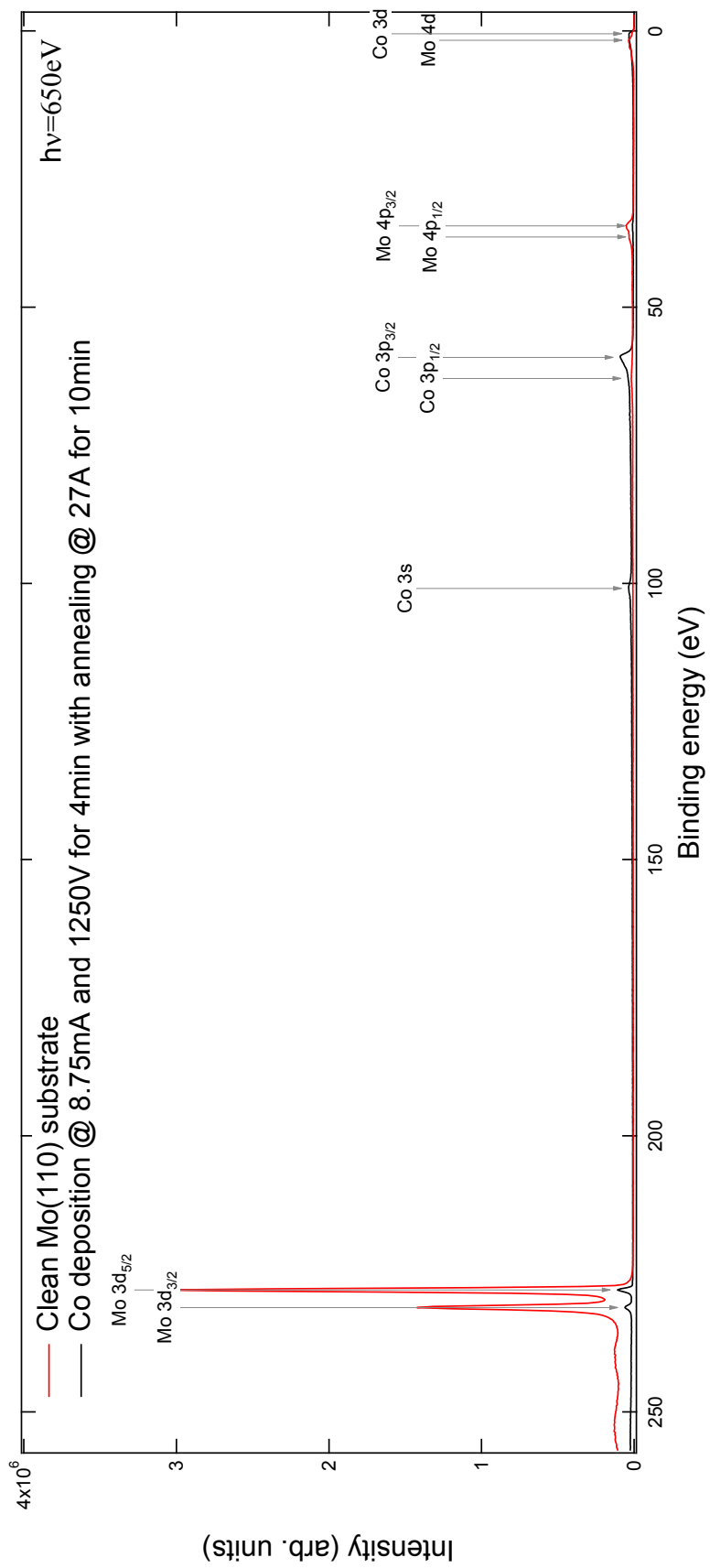


Fig. 4.6 XPS spectra after 4min of Co deposition on Mo(110).

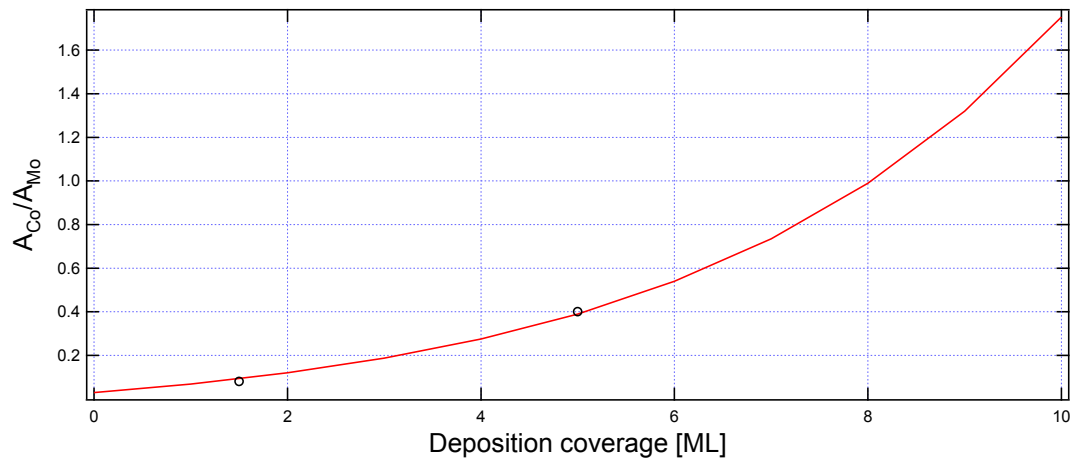


Fig. 4.7 Red line represent expected values of the ratio between areas of Co 3*p* and Mo 3*d* core levels versus thickness of Co thin film on Mo substrate. Circles represents measured area ratio from core level spectra.

Table 4.1 Calculated values of Co 3*p* and Mo 3*d* areas and from measured core level spectra.

Evaporation time	A_{Co}	A_{Mo}	A_{Co}/A_{Mo}	Calculated thickness of deposited film [ML]
4min	306317	3824940	≈ 0.08	1.5
10min	93204	230774	≈ 0.4	5

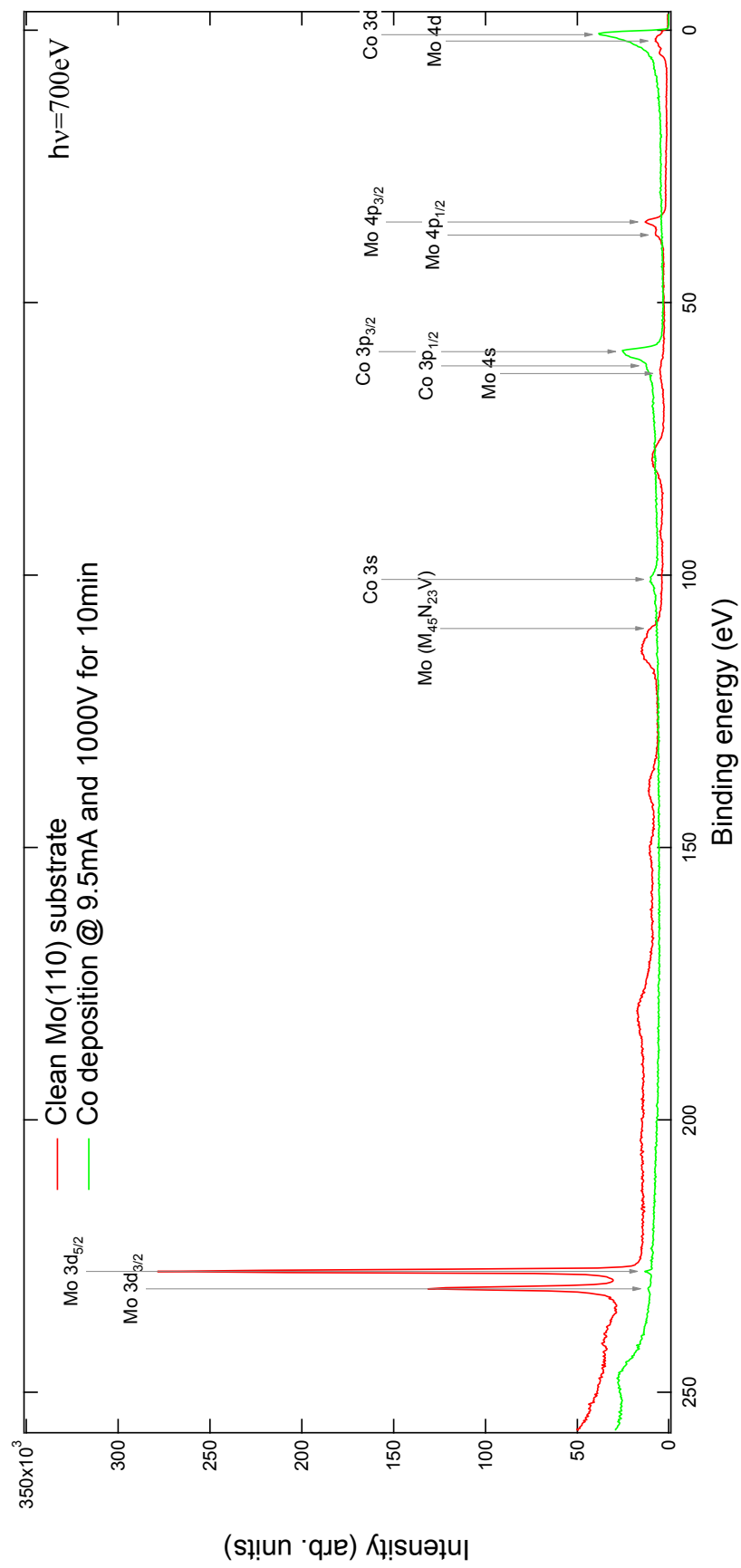


Fig. 4.8 XPS spectra of Co thin film after 10min deposition interval.

5. ARPES study of quantum well states of Co thin film on Mo(110)

Angle-resolved photoemission is an extremely powerful technique for measuring the quantum well states of thin films, because it yields information about the occupied states directly (see Sec. 2.4).

In this section we report the preliminary study of the electronic structure of thin films of Co grown on Mo(110) using the knowledge acquired onto the preparation of Mo(110) surface and Co thin film on Mo(110) presented in the Sec. 3 and Sec. 4. We prepared Co films of different thicknesses using the calibration previously done (see Sec. 4).

In Fig. 5.1 we report the photoemission intensity map (see Sec. 2.4) of 8 ML of Co on Mo(110) along the Γ K direction in the energy range close to the Fermi level (0 eV). In the intensity map we distinguish three electronic structures that disperse parabolically as a function of the k momentum. The structures correspond to three quantum well branches (different n) due to the electron confinement onto 2D Co film.

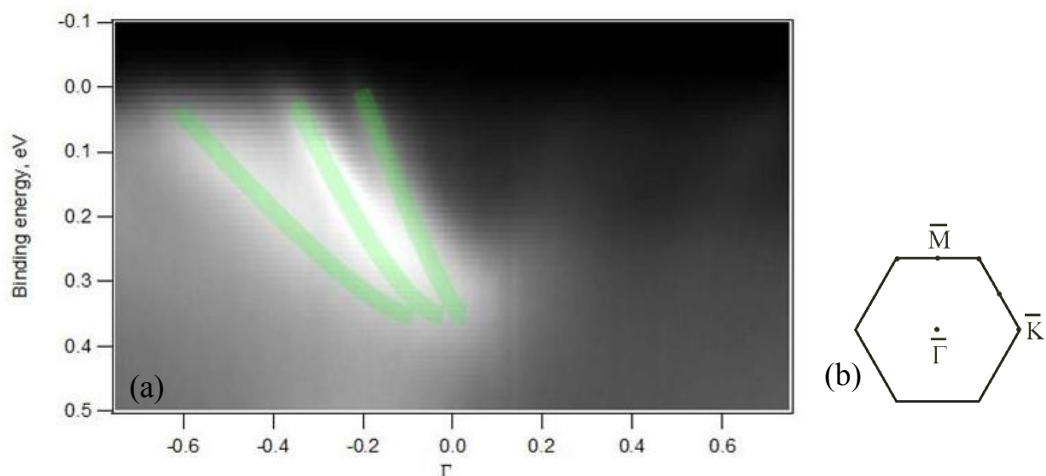


Fig. 5.1 (a) Photoemission intensity map of 8 ML of Co on Mo(110) measured with photon energy 56 eV. (b) Sketch of the surface Brillouin zone of the hcp lattice.

In Fig. 5.2 (a)-(c), we report the photoemission intensity map of 8 ML of Co film on Mo(110) measured as deposited at room temperature (see Fig. 5.2(a)), after 10 minutes of annealing at 400K (see Fig. 5.2(b)) and after a second annealing at 420K done for 10 minutes (see Fig. 5.2(c)). We observe that the quantum well structures become more defined after the subsequent annealing. This is clearly related to an improvement of the crystalline quality of the Co film. As expected (see Sec. 1.2) the reduction of atomic layer fluctuation allows a more precise measurement of the quantum confinement effects.

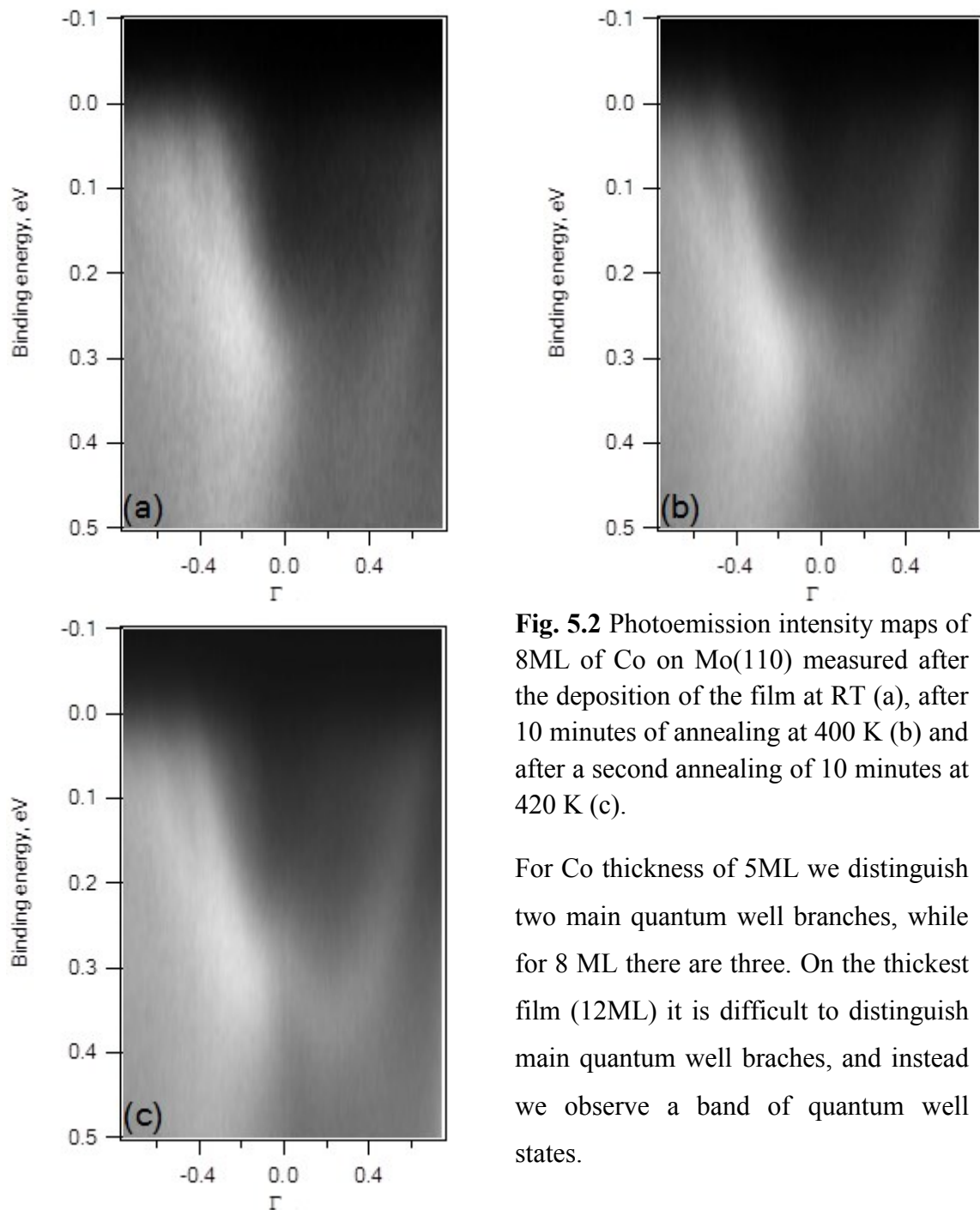


Fig. 5.2 Photoemission intensity maps of 8ML of Co on Mo(110) measured after the deposition of the film at RT (a), after 10 minutes of annealing at 400 K (b) and after a second annealing of 10 minutes at 420 K (c).

For Co thickness of 5ML we distinguish two main quantum well branches, while for 8 ML there are three. On the thickest film (12ML) it is difficult to distinguish main quantum well braches, and instead we observe a band of quantum well states.

As we discussed in the introduction (see Sec. 1.2), by increasing the thickness of the film the energy difference between the quantum well states decreases and peaks become more crowded as the thickness increases.

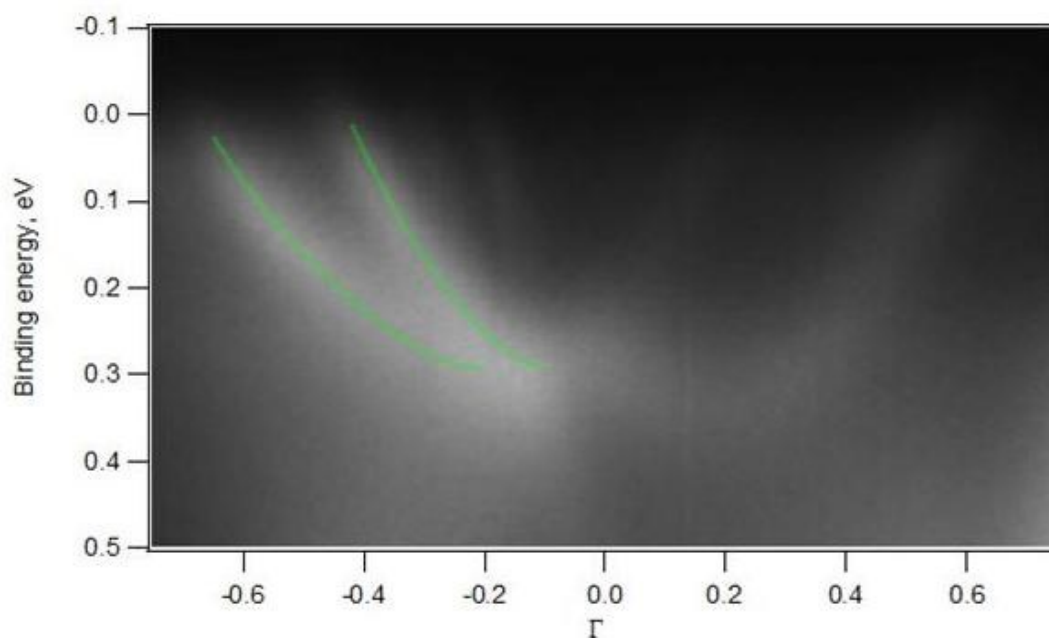


Fig. 5.3 Photoemission intensity map of 5 ML of Co on Mo(110).

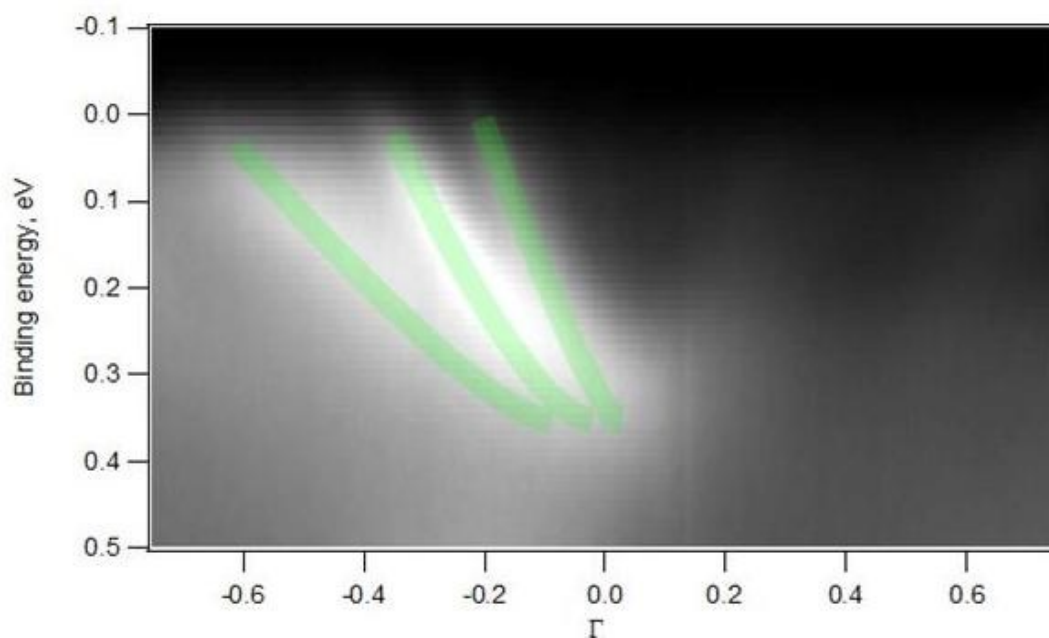


Fig. 5.4 Photoemission intensity map of 8 ML of Co on Mo(110).

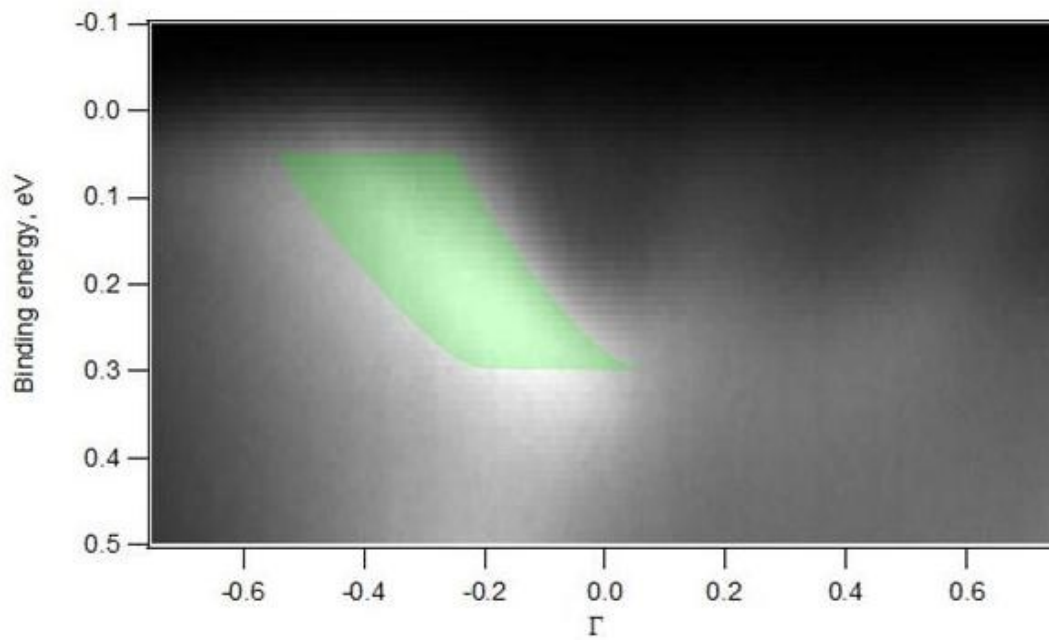
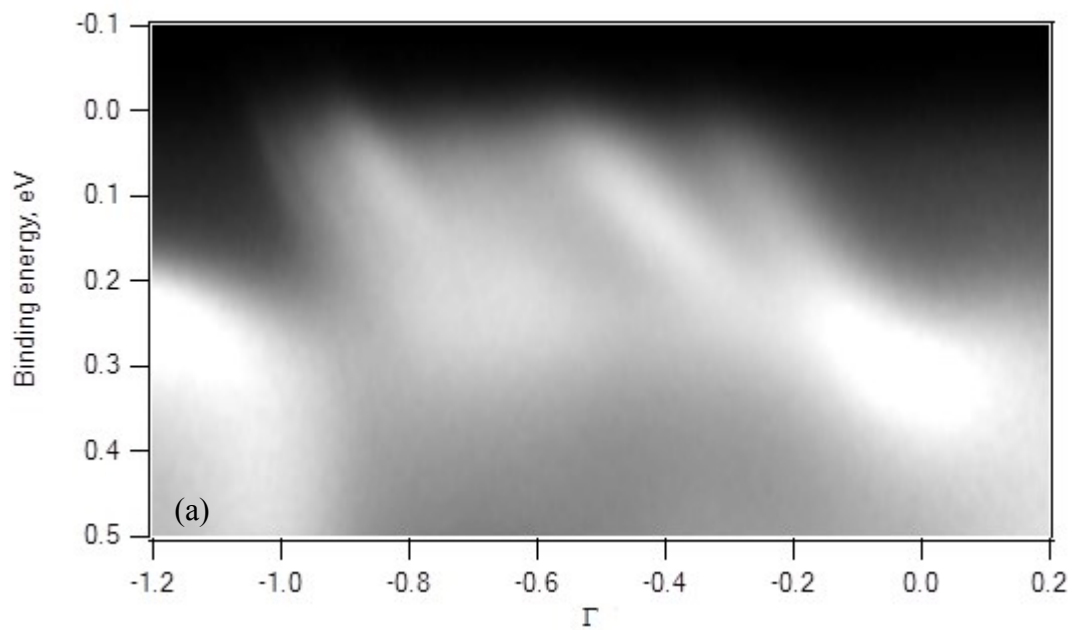


Fig. 5.5 Photoemission intensity map of 12 ML of Co on Mo(110).

On the film thickness of 8 ML we measured the photoemission intensity maps after the magnetization of the Co film (see Fig. 5.6(a) for magnetization up and (b) for magnetization down). The magnetization was done using the set up described in Fig. 2.4. The sample was magnetized in the plane of the Co film and the measurements were acquired along the ΓK direction.



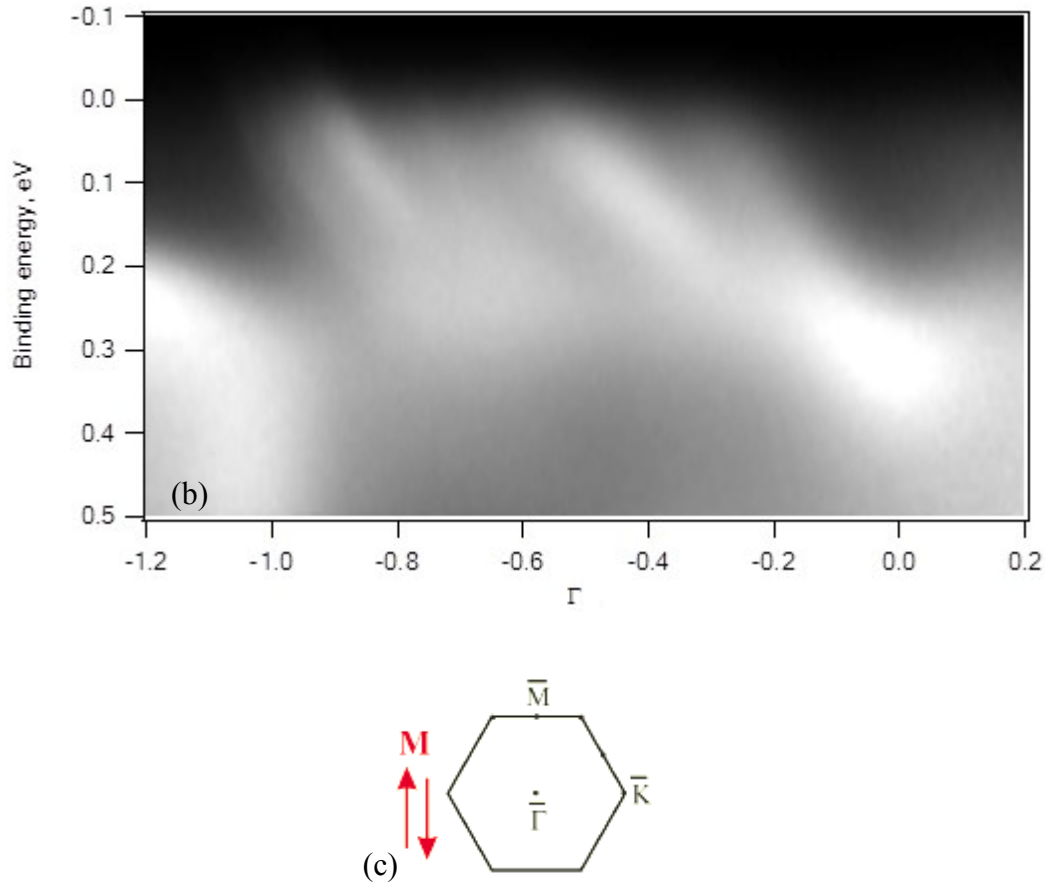


Fig. 5.6 Photoemission intensity map of 8ML of Co on Mo(110) magnetized UP (a) and DOWN (b). In (c) the magnetization directions with respect to the surface Brillouine zone of the hcp lattice.

The two maps do not show up differences in the quantum well states dispersion for the two opposite magnetization direction. In the case of Co thin film on W(110) [15] it was observed that the quantum well dispersion along the $\Gamma\bar{K}$ direction (perpendicular to \bar{M}) for the two opposite magnetization direction were different.

From the study of the electronic structures of Co thin film on Mo(110) we can conclude that the Co quantum well states behaviour does not depend on the spin-orbit effects intrinsic to the Co states. Since the overall electronic hybridization of Co with Mo(110) and W(110) is similar due to the similar atomic and band structures of the two substrates, while the essential difference is the reduction of spin-orbit interaction in Mo, we attribute the previously observed effects in Co/W(110) system to the spin-dependent hybridization.

6. Conclusions

The preparation of Mo(110) surface has been done by measuring, at the different stages of the preparation procedure, the LEED patterns and the XPS spectra. Optimal annealing procedure has been established in order to reduce surface contamination from C and O.

XPS core level measurements and qualitative LEED analysis were used to characterize the preparation of Co thin film on Mo(110). The thickness calibration was done measuring the LEED patterns and the Co and Mo core level intensity as a function of evaporation duration.

On photoemission intensity maps of 5 ML and 8ML Co film thickness we observed quantum well states. The quality of the quantum well states was improved by annealing the Co film at about 400 K because of an improvement of the crystalline quality of the film.

An increase of the number of the quantum well branches has been observed by increasing the film thickness.

The quantum well states of the Co film do not present differences for different direction of the magnetization.

In conclusion, with the present work we find the experimental condition for the growth of atomically uniform Co film on Mo(110) that supports quantum well states. The lack of magnetization dependence of the quantum well dispersion is a preliminary result that will serve for further ARPES study and comparison with the results obtained for the system Co on W(110).

Bibliography

- [1] E. Lundgren, U. Johansson, R. Nyholm, and J. N. Andersen, *Phys. Rev. B* 48, 5525 (1993).
- [2] K. Radican, N. Berdunov, G. Manai, and I. V. Shvets, *Phys. Rev. B* 75, 155434 (2007).
- [3] Charles L. Roe, Kirk H. Schulz, *Surf. Sci.* 446, 254 (2000).
- [4] P. Hofmann, *Lecture notes on surface science*, (2005).
- [5] K. Oura, V. G. Lifshits, A. A. Saranin, A. V. Zotov, *Surface science (An introduction)*, 2003.
- [6] A. Mikkelsen, L. Ouattara, E. Lundgren, *Surf. Sci.* 557, 109 (2004).
- [7] Jian-Wei He and D. Wayne Goodman, *Surf. Sci.* 245, 29 (1991).
- [8] Hans Lüth, *Solid Surfaces, Interfaces and Thin Films*, Graduate texts in physics, 2010.
- [9] <http://www.diamond.ac.uk/Home/Technology/Components.html>.
- [10] http://www.vgscienta.com/_resources/File/Catalogue_Sections/VGScienta_Surface_Science_Instruments.pdf.
- [11] <http://origin-ars.els-cdn.com/content/image/1-s2.0-S0368204810000940-gr1.jpg>.
- [12] F.J. Himpsel, J.E. Ortega, G.J. Mankey, R.F. Willis, *Adv. Phys.* 47, 511–597 (1998).
- [13] J. E. Ortega and F. J. Himpsel. *Phys. Rev. Lett.* 69, 844 (1992).
- [14] S. D. Bader and S.S.P. Parkin, *Annu. Rev. Condens. Matter Phys.* 1, 71 (2010).
- [15] P. Moras et al., 2013 private communication.

- [16] Albert Messiah, *Quantum Mechanics* (Vol. I), English translation from French by G. M. Temmer. North Holland, John Wiley & Sons (1966).
- [17] T.-C. Chiang, Surf. Sci. Rep. 39, 181 (2000).
- [18] J. Prokop, D. A. Valdaitsev, A. Kukunin, M. Pratzner, G. Schönhense and H. J. Elmers, Phys. Rev. B 70, 184423 (2004).
- [19] E. Bauer and Jan H. van der Merwe, Phys. Rev. B 33, 3657 (1986).
- [20] <http://www.elettra.trieste.it/lightsources/elettra/elettra-beamlines/vuv/vuvdescription.html>.
- [21] J. J. Yeh and I. Lindau, Subshell photoionization cross section At. Data Nucl. Data Tables 32, 2 (1985).
- [22] Charles Kittel, Introduction to Solid State Physics, 8th edition, John Wiley & Sons (2005).